TIMED Doppler Interferometer on the Thermosphere Ionosphere Mesosphere Energetics and Dynamics satellite: Data product overview

R. Niciejewski,[1] Q. Wu,[3] W. Skinner,[1] D. Gell,[1,2] M. Cooper,[1] A. Marshall,[1] T. Killeen,[3] S. Solomon,[3] and D. Ortland[4]

Received 1 November 2005; revised 6 March 2006; accepted 26 May 2006; published 9 November 2006.

[1] The TIMED Doppler Interferometer (TIDI) performs the measurement of upper atmospheric winds on the Thermosphere Ionosphere Mesosphere Energetics and Dynamics (TIMED) satellite. This is an optimized single etalon Fabry Perot interferometer that records the slight Doppler shift of individual emission features of the O_2 (0,0) atmospheric band. The interferometer operates at a 100% duty cycle obtaining neutral wind altitude profiles on a global basis. The measurements are synoptic and provide an uninterrupted long-term climatological record of the dynamics in the mesosphere and lower thermosphere regions. The data products from TIDI include (1) apparent line of sight winds and integrated brightness, (2) inverted line of sight winds and volume emission rate, and (3) inverted horizontal neutral wind fields on an evenly spaced track angle/altitude grid. The data products demonstrate an interannual variability in the tidal structure of the mesosphere and the lower thermosphere and an inherent daily geophysical variance.

Citation: Niciejewski, R., Q. Wu, W. Skinner, D. Gell, M. Cooper, A. Marshall, T. Killeen, S. Solomon, and D. Ortland (2006), TIMED Doppler Interferometer on the Thermosphere Ionosphere Mesosphere Energetics and Dynamics satellite: Data product overview, *J. Geophys. Res.*, *111*, A11S90, doi:10.1029/2005JA011513.

1. Introduction

[2] The TIMED Doppler Interferometer (TIDI) flying aboard the Thermosphere Ionosphere Mesosphere Dynamics and Energetics (TIMED) satellite is the last in a long and unique series of satellite-borne scientific optical instruments built and commissioned at the Space Physics Research Laboratory (SPRL) of the University of Michigan. The design philosophy for TIDI is based on experience gathered by SPRL from over 30 years of performing comprehensive scientific optical observations from low Earth orbiting satellites. Initial space flight hardware design experience was collected from the Visible Airglow Experiment (VAE) flown on Atmosphere Explorers C, D, and E [*Hays et al.*, 1973], with launch dates of 13 December 1973, 6 October 1975, and 20 November 1975, respectively. The experiment consisted of relatively simple optical devices: a pair of photomultiplier tubes with a shared filter wheel designed to observe the terrestrial limb airglow and aurora through separate orthogonally oriented telescopes. Initial high spectral resolution observations of the limb to measure the Doppler shift of airglow and auroral emissions in the thermosphere were conducted with a Fabry Perot interferometer flown on the Dynamics Explorer B satellite [*Hays et al.*, 1981] launched on 3 August 1981. The experiment incorporated a single etalon and a unique image plane detector optimized to match the circular Fabry-Perot fringe pattern and measured the meridional wind component in the upper thermosphere. Stratospheric wind measurements were first conducted with the High Resolution Doppler Interferometer [*Hays et al.*, 1993] launched on the Upper Atmosphere Research Satellite on 12 September 1991. This experiment consisted of a triple etalon design with a gimbaled telescope permitting limb viewing both fore and aft of the satellite track. Low tangent altitude wind measurements were obtained from analysis of absorption features.

[3] The TIMED satellite, launched on 7 December 2001, included four scientific packages to observe the interaction of solar influences on the upper atmosphere [*Yee et al.*, 2003]. Neutral winds in the mesosphere and lower thermosphere are measured with TIDI. Spectral features are resolved with TIDI with sufficient resolution to measure Doppler shifts as small as a few m/s. Daytime and nighttime winds are determined from analysis of O_2 (0,0) Atmospheric band lines. The limb is sampled simultaneously at four orthogonal directions by vertically scanning telescopes that are oriented in a cross-shaped pattern 45 degrees to the satellite velocity vector. The four input beams are then shaped by optical fibers into a quadrant that is collimated before passing through a dual filter wheel. The optical design permits the use of interference filters that have a spectral width as narrow as 0.3 nm. The quadrant retains the individual arc structure that represents each of the four telescope inputs plus a fifth calibration lamp input. The

[1]Space Physics Research Laboratory, University of Michigan, Ann Arbor, Michigan, USA.
[2]Now at Southwest Research Institute, San Antonio, Texas, USA.
[3]National Center for Atmospheric Research, Boulder, Colorado, USA.
[4]NorthWest Research Associates, Bellevue, Washington, USA.

0148-0227/06/2005JA011513

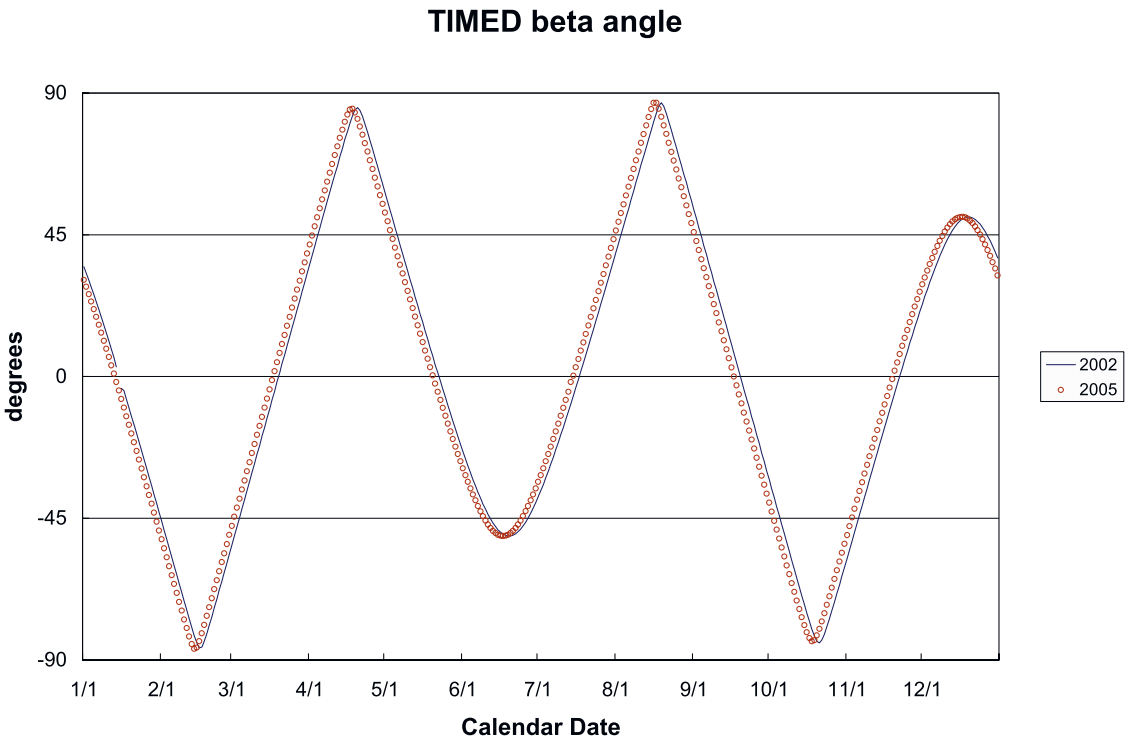

Figure 1. The TIMED beta angle for the years 2002 and 2005. The beta angle is the angle between the Earth-Sun line and the complement to the normal to the orbital plane. The beta angle has shifted by one day between 2002 and 2005. TIMED yaw maneuvers occur during the middle of odd numbered months. Maximum beta angle occurs during even numbered months, with the greatest values (~86 degrees) occurring in mid February, April, August, and October.

beam is then expanded and is passed through a single etalon. Imaging optics then pass the beam to a circle to line imaging device [*Hays*, 1990], a mirror in the shape of a tapered cone which transforms the quarter-circle fringe pattern to a series of spectral lines. The detector then samples simultaneously the four individual sky fringe patterns, each approximately 0.32 cm^{-1} wide onto 22 (telescope 4) to 54 (telescope 1) channels. Slightly more than one free spectral range is sampled for each telescope scene eliminating the need to tune the etalon in flight. The resultant instrumental resolution is roughly 0.03 cm^{-1}.

[4] *Killeen et al.* [1999] presented a prelaunch overview of TIDI describing the instrument, optical components, and system characteristics. Thermal, detector, and optical performance for the first 18 months of on-orbit operations are described by *Skinner et al.* [2003]. Only the most salient details regarding on-orbit instrument operation and detector geometry are included here. The next section of this paper describes the implications for TIDI of the TIMED orbit, followed by a discussion of the different level TIDI wind products.

2. TIDI Mission

2.1. On Orbit Fundamentals

[5] TIMED was launched from Vandenberg Air Force Base into a circular orbit at a nominal altitude of 625 km with an inclination angle of 74 degrees. The mission had an initial 2-year lifespan but since has been operating under a 3-year extended NASA program. The orbital parameters were chosen to "freeze" the Earth-viewing geometry on an annual cycle for the lifetime of the mission. Essentially, TIDI returns to the same Local Solar Time (LST) and latitude coordinates of the volume of space viewed on any calendar date exactly 1 year earlier. The orbit is optimized to perform long-term synoptic measurements of the important basic parameters of the mesosphere and thermosphere. The beta angle, describing the angle between the Earth-Sun line and the complement to the normal to the satellite orbital plane is shown in Figure 1. The beta angle trend shows that the orbit has shifted by 1 day in 3 years, insignificant in terms of understanding the long-term variation of tidal winds in the upper atmosphere. Figure 1 also indicates that there are 6 zero crossings during a year, occurring in the middle of odd-numbered months. On these dates, the TIMED satellite undergoes a yaw maneuver, changing from forward flight to backward flight or vice versa. For TIDI, the yaw maneuvers keep the orientation of the telescopes constant: warmside telescopes remain on the sunward side following a yaw maneuver and coldside telescopes remain on the shadow side. The daily LST coverage (which is nearly constant as a function of track angle for any given day) advances 12 min per day, indicating that TIDI can observe winds for a full 24-hour solar day between yaw maneuvers using combined ascending and descending mode data.

[6] Another important scientific consequence for TIDI of the chosen satellite orbit is true global coverage of the

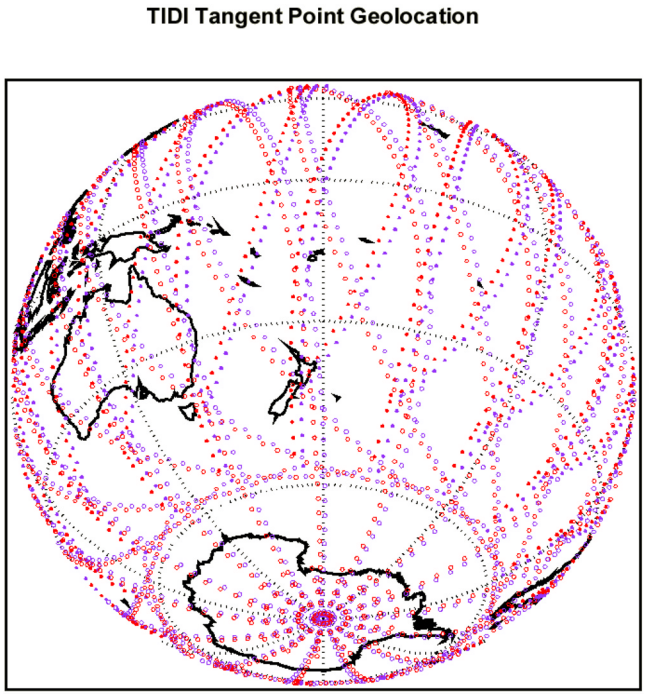

Figure 2. Geolocation of the TIDI tangent point limb intercepts for one day's set of orbits. The open circles refer to the two telescopes viewing on one side of the TIMED satellite, while the closed circles refer to the opposite side. Red and blue coloring refer to warmside and coldside, respectively. A consequence of the viewing geometry and the satellite orbit characteristics is that at a latitude extreme, two telescopes can view up to and slightly over a pole while the other two provide a detailed latitudinal coverage near 57 degrees latitude.

neutral wind, a first for the mesosphere/lower thermosphere (MLT) region. The four telescopes are oriented at 45 degrees to the satellite velocity vector and as a result, when the satellite is at its greatest northern or southern latitude, one pair of either the coldside or the warmside telescopes will actually view slightly over the northern or southern pole, depending upon the flight direction. The geometry is described in Figure 2 for the Southern Hemisphere, where the volume of space at the Earth's limb viewed by a telescope is shown with a small open circle at its corresponding geolocation. The set of orbits shown in Figure 2 corresponds to 1 day's coverage, with a time interval of approximately 100 min between individual orbits. This contrasts with the latitude limits of ±70 degrees for HRDI [*Hays et al.*, 1993].

[7] TIDI acquires more than 50,000 airglow spectra per telescope in 1 day. The spectra are collected in vertical scans that require ~100 s per cycle. A representation of a scan is illustrated in Figure 3, which shows that TIDI obtains vertical limb profiles through the airglow layers from all four telescopes simultaneously. A typical pair of day/night modes is described in Table 1. The gain settings, in terms of the raw measured analog/digital unit (ADU), are set to optimize the signal levels for day and night operations, 40 e-/ADU and 10 e-/ADU, respectively. Read noise levels, measured on-orbit, are approximately 15 e- RMS for both gains [*Skinner et al.*, 2003], implying that the charge coupled device (CCD) detector is operating with ~1 ADU read noise. The onboard TIDI CPU restarts every day at 0000 UT and reads the two nominal operational modes. These modes may change on a daily basis, if necessary, though the operational philosophy is to conduct long-term synoptic measurements of the MLT region. Once a week, the dayside portions of the first three orbits are modified to perform white light normalization calibration runs, basically lowering the altitude scan limits to force TIDI to image Rayleigh scattered sunlight from the lower atmosphere. At high beta angles, the two modes are modified slightly to improve the signal to noise ratio of the measurement. The duty cycle for TIDI is 95% for airglow science acquisition and 5% for instrument calibration runs. The latter are performed when the satellite enters dusk, which occurs at least 14 times per day. A full daily set of calibration runs consists of 5-min segments which when completed at the end of a day provide a monitor of detector sensitivity to both white light and a neon source, instrument drift and finesse, CCD engineering characteristics, and electronic bias. TIDI has acquired airglow spectra in the current operational mode for every day since 13 February 2002, with very few exceptions due to satellite maneuvers and special TIDI engineering tests.

[8] TIDI sensitivity to white light has been described by *Skinner et al.* [2003] up to mid-2003. The sensitivity to narrow spectral lines is shown in Figure 4 and is similar in nature to that of white light. The sensitivity of TIDI decreased rapidly following orbital insertion. Two special maneuvers were conducted in early 2003 that warmed TIDI sufficiently to reverse the deterioration process. TIDI continues to show improvement in sensitivity, though the rate of improvement has slowed to approximately 10%/year. Fits to the spectral line calibration runs may be used to estimate the long-term drift, as shown in Figure 5. Relative to initial runs obtained shortly after instrument turn-on in orbit, TIDI appears to have drifted approximately 100 m/s in spectral space. Currently, daily calibration lamp measurements have a fit uncertainty of ~1 m/s, compared to ~10 m/s for fits obtained in early 2003. In summary, the performance of TIDI continues to improve after the two special maneuvers of early 2003, though the rate of improvement has slowed.

2.2. Data Products

2.2.1. Overview

[9] TIDI data products are organized into four different levels. These are described in Table 2. Telemetry data are available to the TIDI Payload Operations Center at the University of Michigan on the second day following data acquisition, and these are routinely converted into a Level 0 product. The final set of spacecraft attitude information is available on the third day following data acquisition, and these are necessary to complete the reduction into TIDI data products at Levels 1, 2, and 3.

[10] Light is incident upon the TIDI etalon from five different scenes that are formed into a quadrant with fiber optics. The region of the detector that is then illuminated is illustrated in Figure 6, which includes all the different binning or imaging geometries employed by TIDI. Two different binning strategies have been used for airglow

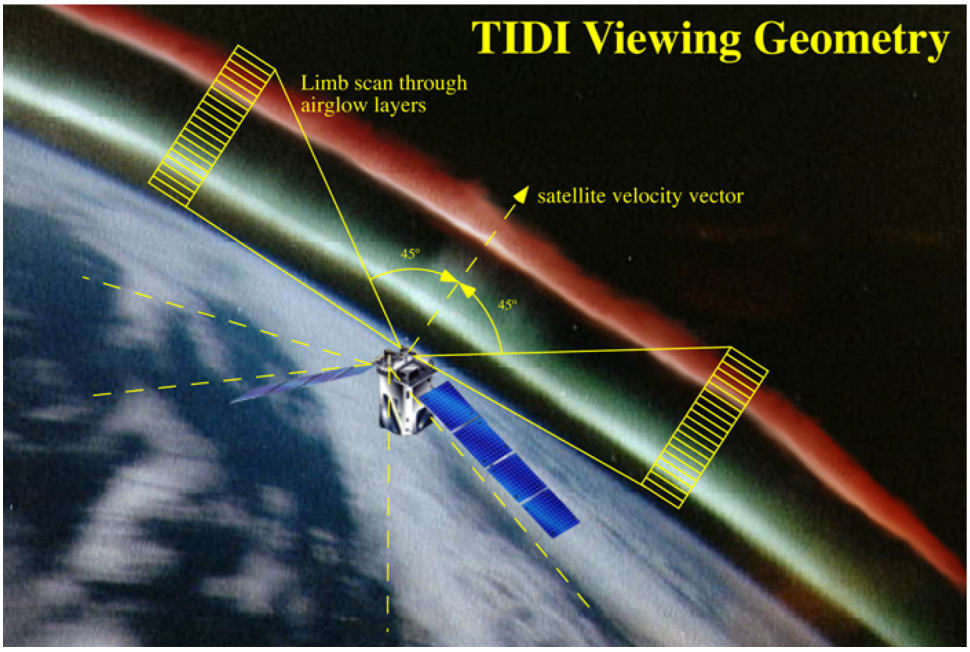

Figure 3. Schematic diagram illustrating a TIDI vertical scan sequence. During nominal science operations, all telescopes scan through the airglow layers simultaneously.

spectra, an equal wavelength and an equal area set. The former provides spectra as a function of theta (or radius) squared which is directly related to wavelength [*Niciejewski et al.*, 1994], while the latter uses a common (2 column × 81 row) binning strategy to create 255 contiguous spectral channels. Calibration runs are obtained either as individual images (600 column × 50 row) or binned spectra (155 channels of 1 × 40 summed pixels). A white calibration lamp image, beneath the boxes, is an inflight image that represents the result from the circle to line translation [*Hays*, 1990] of a Fabry Perot fringe pattern. The vertex of the resultant linear TIDI fringes, identically the "bull's-eye" of the original circular fringes, is physically located in column 862. The vertical striping features are individually resolved fiber optic bundles that are translated into all TIDI spectra. The four boxes to the left of the calibration field represent the location of individual telescope scenes, all of similar free spectral range, but of different linear extent, while the

Table 1. Nominal Dayside and Nightside Operational Science Modes[a]

Wavelength, nm	Fw 1	Fw 2	Integ, s	Cal	Exp Count	(B)in/(I)mage	Bin Table	(A)ll Telescopes	Alt Low, km	Alt High, km	Alt Step, km	Shutter
						Dayside						
765.07	4	1	0.75	off	1	B	1	A	70.0	100.0	1.25	open
000.00	4	1	0.75	off	1	B	1	A	100.0	100.0	1.25	close
763.78	8	1	0.75	off	1	B	1	A	80.0	112.5	1.25	open
000.00	8	1	0.75	off	1	B	1	A	112.5	112.5	1.25	close
000.00	1	8	0.00	off	1	B	1	A	115.0	115.0	1.25	close
764.00	6	3	0.75	off	1	B	1	A	80.0	120.0	1.25	open
000.00	6	3	0.75	off	1	B	1	A	120.0	120.0	1.25	close
557.70	7	1	0.75	off	1	B	1	A	148.0	151.0	1.50	open
000.00	7	1	0.75	off	1	B	1	A	151.0	151.0	1.50	close
						Nightside						
000.00	8	1	3.0	off	1	B	1	A	80.0	80.0	2.50	close
763.78	8	1	3.0	off	1	B	1	A	80.0	105.0	2.50	open
765.07	4	1	3.0	off	1	B	1	A	80.0	105.0	2.50	open
557.70	7	1	3.0	off	1	B	1	A	93.0	99.0	3.00	open
000.00	7	1	3.0	off	1	B	1	A	105.0	105.0	2.50	close
000.00	6	3	1.0	off	2	B	1	A	80.0	80.0	2.50	close
764.00	6	3	1.0	off	2	B	1	A	80.0	105.0	2.50	open
000.00	6	3	1.0	off	1	B	1	A	105.0	105.0	2.50	close
000.00	1	8	0.0	off	1	B	1	A	98.5	98.5	2.50	close

[a]On orbit, the TIDI CPU reads one row at a time to determine filter wheel position (wavelength, fw1, fw2), scene dwell period (integ), calibration lamp status (cal), scene dwell repeats (exp count), type of CCD output (binned or image), binning strategy (bin table), the number of telescopes to operate (all telescopes), the vertical scanning strategy (alt low, alt high, alt step), and the telescope shutter position (shutter). A wavelength of 000.00 indicates a dark count measurement. An integration period of 0.0 s indicates an electronic bias measurement.

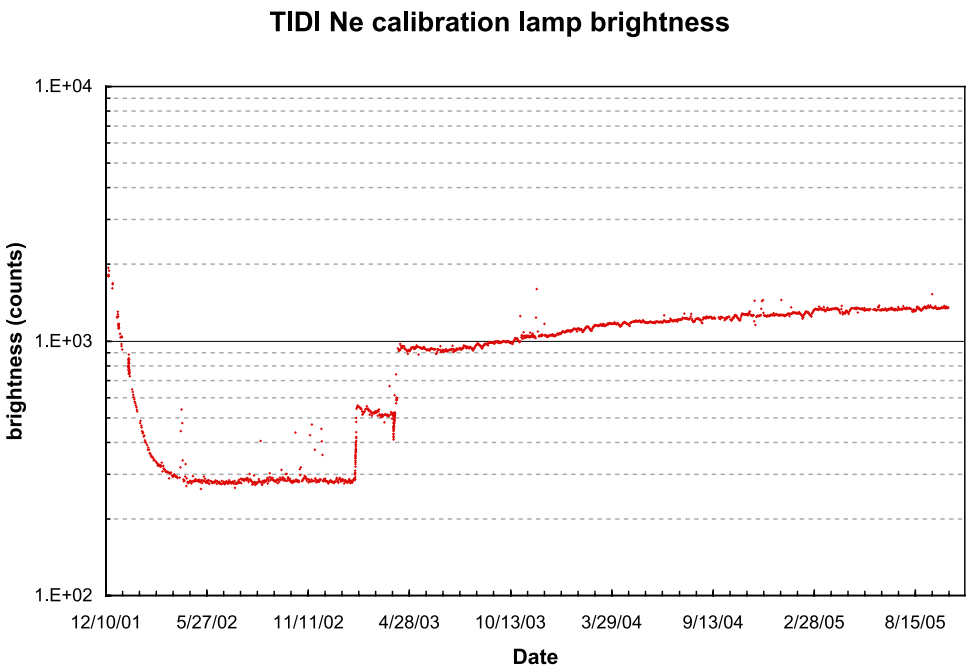

Figure 4. The long term sensitivity trend of TIDI to the 630.4 nm line from the onboard neon spectral calibration lamp. The two jumps in early 2003 correspond to improvements resulting from special TIMED maneuvers.

gaps between telescope scenes represent the linear translation of 50-micron wide stops meant to isolate the fiber optic strands into separate telescope images or spectra.

[11] Though TIDI acquires synoptic wind measurements of the MLT only, several engineering runs have been performed to test the low light level sensitivity of the interferometer against a high background level by observing upper thermospheric dayglow emissions. Two example spectra from these airglow line surveys are shown in Figure 7. The series of spectra shown for OI (6300Å) (top) and OI (8446Å) (bottom) were acquired near the September equinox of 2003. Both emissions occur at middle

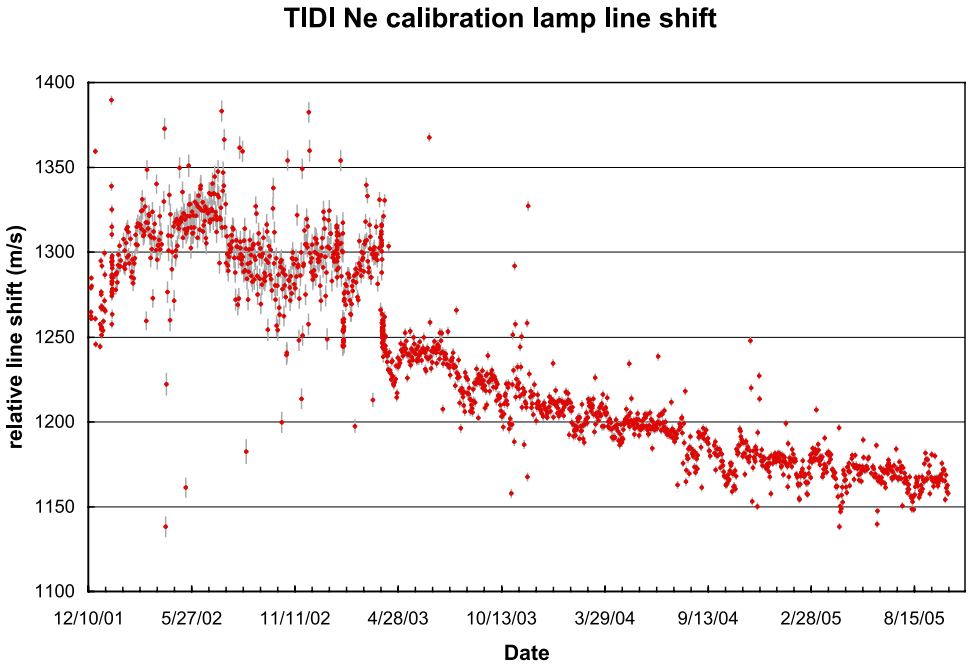

Figure 5. The long-term drift of TIDI, determined from fits to the 630.4 nm neon spectral line measured during daily calibration runs. The relative line shifts are shown with the uncertainty of the fit, the latter currently at ~1 m/s but as high as 10 m/s prior to the early 2003 special TIMED maneuvers.

Table 2. A Description of the Different TIDI Data Products[a]

TIDI Data Product	Description	Geophysical Quantities
Level 0	Telemetry data that has been reconstructed. The product is unprocessed instrument data at full resolution.	(1) raw spectra
Level 1	Level 0 data that have been processed into sensor units. The product is time referenced and annotated with ancillary information including tangent point position, solar zenith angle, and local solar time. Geophysical data have been fully corrected for instrumental effects.	(1) calibrated spectra (2) line of sight winds (3) airglow brightness
Level 2	Level 1 spectra that have been processed into vertical profiles of geophysical quantities on a uniform altitude grid. These vertical profiles are at the highest available horizontal and temporal resolution.	(1) inverted wind profiles along a line of sight (2) inverted volume emission rate profiles
Level 3	Level 2 data that have been mapped onto a uniform time and position grid.	(1) inverted vector wind profiles

[a]Data from Levels 1, 2, and 3 are available to the community 3 days following data acquisition.

to upper thermosphere altitudes. The orbital geometry placed TIMED near the local noon/midnight meridian during the test sequence, and these examples were acquired at high northern latitudes near the region where the local solar time changes by 12 hours, that is near twilight conditions. As TIDI enters twilight, the line of sight columnar brightness of the OI (6300Å) emission decreases rapidly. A slight wavelength shift is evident indicating a change in the line of sight Doppler speed. Figure 7 shows the sum of several minutes worth of individual spectra and illustrate the superb low noise capability of TIDI in the presence of a high daytime background.

[12] The triplet emission of OI (8446Å) is not completely resolved by TIDI. The triplet features are expected at 8446.26, 8446.38, and 8446.76 Å in the airglow [*Hecht et al.*, 1985]. The ratio of expected signal brightness of the three lines is 1/9:5/9:3/9 from blue to red. The interpretation of the TIDI spectra begins by assigning the channel position of the brightest line with the anticipated brightest component of the triplet. The free spectral range of TIDI may be absolutely prescribed by knowledge of only the etalon gap spacing, which is 2.2 cm. This converts to a free spectral range of 0.162 Å at 8446 Å, which creates order ambiguity for the 8446 oxygen triplet, placing the weak blue line at (8446.26 + 0.162) Å and the stronger red line at (8446.76 − 2. × 0.162) Å, or 8446.42 and 8446.43 Å, respectively. Assuming that the strong middle line appears at 8446.38 Å, the two anticipated companion lines appear as an unresolved feature in the TIDI spectra near 8446.425 Å for the first two dusk spectra and become mixed with noise levels as the satellite moves into deeper night. As far as is known, these are the first ultra-high-resolution measurements of OI

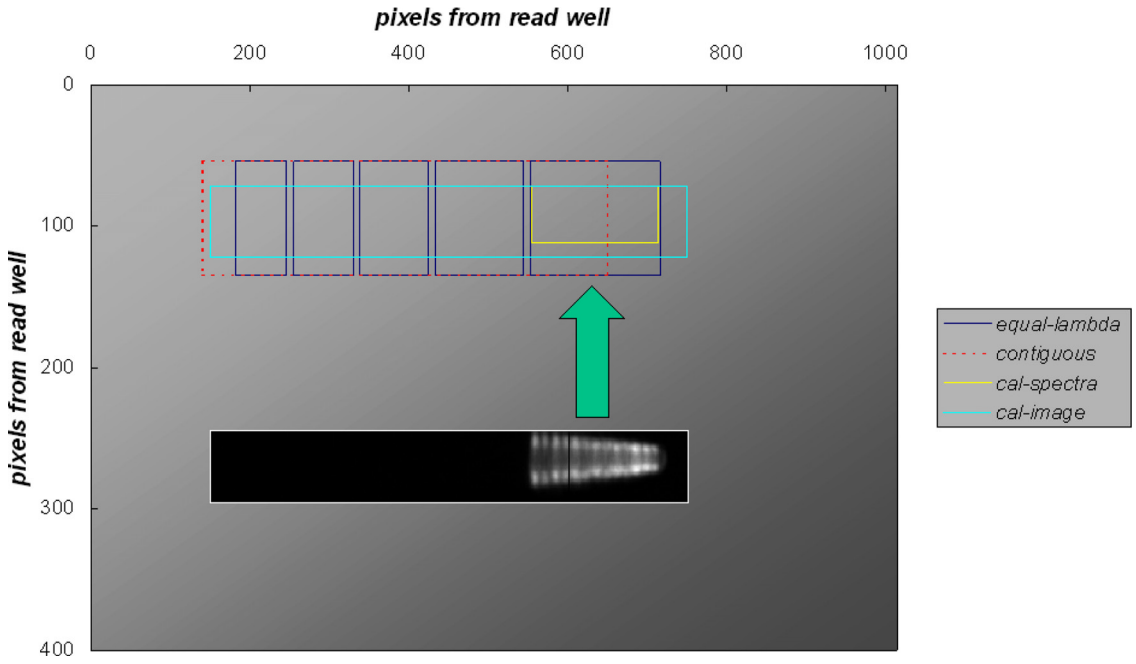

Figure 6. A schematic of the portion of the CCD that is used to view airglow and calibration scenes. The "equal-lambda" region outlines the four telescope fields with the single calibration field on the far right. Seams in the optical fiber bundle separate the five scenes. The contiguous region has been used for airglow measurements since 13 February 2002, and includes samples in the seam areas. Calibration runs are performed both as images (cal-image) and as spectra (cal-spectra). An in-flight white light calibration image is shown with an arrow indicating its physical location on the CCD. The narrowing of the vertical extent of the image points to a vertex at column 862.

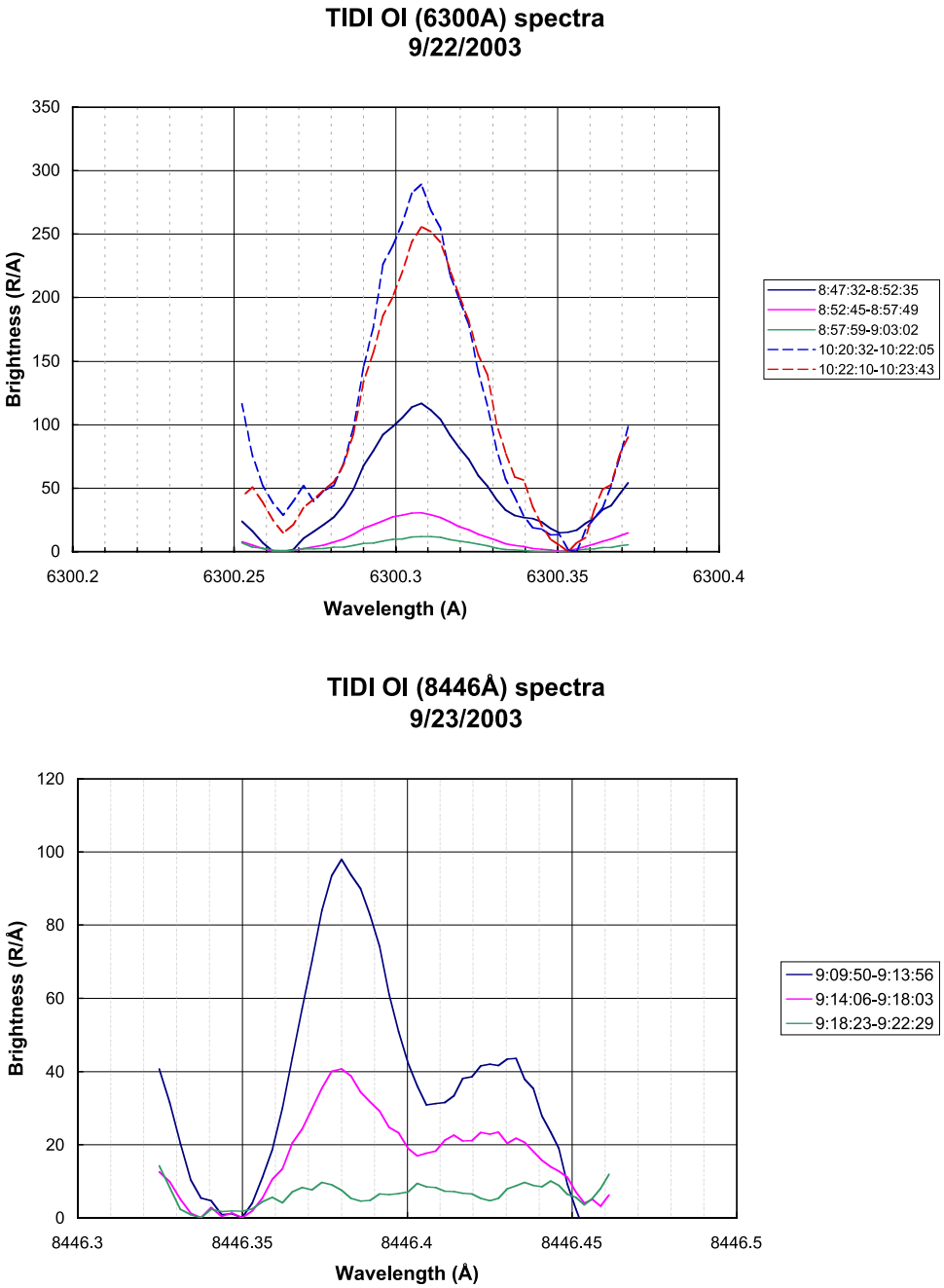

Figure 7. Sample results from TIDI airglow line surveys. (top) OI (6300Å) spectra. (bottom) OI (8446Å) triplet spectra. The spectra for both cases were acquired during dim daylight conditions as TIMED approached dusk. Only telescope 1 spectra are shown. For each case, the spectra are sums of several individual measurements acquired with an integration period of 0.5 s. The triplet OI (8446 Å A) emission is not completely resolved, with the two weaker components suffering order ambiguity and appearing near 8446.425 Å. The uncertainty of the spectral points in these averages is on the order of a few R/Å.

(8446Å) airglow emission spectra capable of providing Doppler wind shifts in the terrestrial atmosphere.

2.2.2. Level 0 Product

[13] An example of a Level 0 TIDI spectrum acquired during nominal science operations is shown in Figure 8. This spectrum was acquired with a 1.0-s integration at 40 e-/ADU. Each of the individual fields are outlined in Figure 8, with each telescope field showing features from the O_2 At (0,0) P9 lines. The CCD operates at −83°C, and so the contribution from thermal noise generation per CCD pixel to the final spectrum will be negligible, approximately 1 e-/spectral channel. The measured electronic read noise is less than the quantization per ADU, implying that the dominant noise component in the spectrum will simply be photon noise, which follows a Poisson distribution. Assuming unity quantum efficiency in the translation of

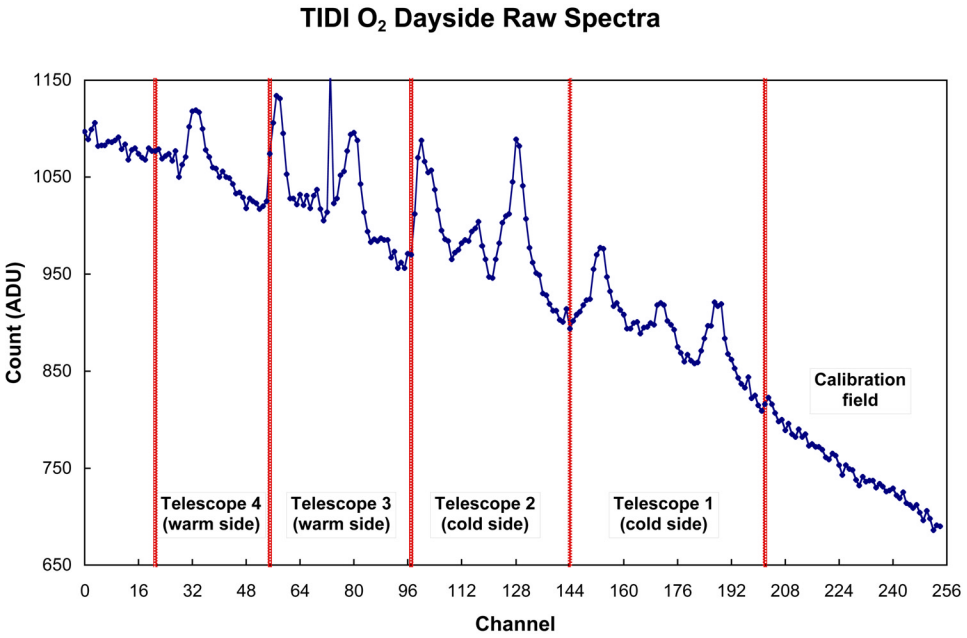

Figure 8. A sample Level 0 dayside O_2 Atmospheric (0,0) P9 spectrum obtained by TIDI. The integration period was 1.0 s at a gain setting of 40 e-/ADU. The individual telescope and calibration scenes are as defined in Figure 6. The data have had no corrections applied to the spectrum. A cosmic ray strike is shown at channel 73.

photons to electrons by the CCD, the noise level of this spectrum is about 5 ADU suggesting a signal to noise ratio (SNR) of over 30 for the brightest peaks.

[14] A longer period of Level 0 data is shown in Figure 9. Here, the response of TIDI channel 75 for a 12-hour period describes the orbital variation in brightness from dayside to night. Closer examination of a shorter 2-hour period allows viewings of each 100 second vertical scan, where each scan samples the airglow layer from the bottom upward. Short data gaps at dusk correspond to calibration runs where no airglow spectra were collected.

2.2.3. Level 1 Product

[15] There are several important considerations in reducing the TIDI data to Level 1. The goal is to remove all instrumental and satellite-induced artifacts from the data sets. In terms of instrumental artifacts, there are several separate operations that are applied to the spectra prior to determining the line of sight wind. The spectra must be (1) checked for cosmic ray strikes, (2) background corrected, (3) normalized with a white light calibration, and (4) converted to absolute brightness units.

[16] Comparing short time series of spectra, as shown in Figure 8, easily identifies cosmic ray noise. The airglow spectral peaks will not shift greatly from one spectrum to the next and so it is quite simple to identify and mark spikes in the data. Cosmic ray spikes are the least invasive noise source for space-based CCDs. Noise related to passage through the South Atlantic Anomaly and to energetic solar events are also evident in raw TIDI spectra. The former are easily identified by satellite geolocation, flagged, and not used in any further data reduction. The latter have only been observed during extreme events such as during the solar superstorm of late October and early November 2003. Spectra were contaminated when the TIDI detector flew through the auroral oval at high latitudes and the ring current region at equatorial latitudes.

[17] Figure 8 also indicates that an intensity gradient in spectral space exists for the TIDI background. Background measurements are accumulated frequently by TIDI, as shown in Table 1 and Figure 9, by closing all telescope shutters. Though it is possible to remove the background by simple differencing against airglow spectra, this operation will enhance noise levels. TIDI models the time/spectral behavior of the background using a fifth-order set of empirical orthogonal functions. This assumes that the background is the sum of an average level plus a linear combination of several basis functions. The functions consist of eigenvalue/eigenvector pairs. The basis vectors for these functions are calculated from background data collected over an entire yaw cycle. In the processing for each day of TIDI data, a mean background spectrum is determined and removed from all background spectra. The residuals are then processed with the basis vectors to determine the multiplicative coefficients. Airglow spectra are then corrected for background levels by interpolating model background spectrum from either side of the sky measurement. This model has proven to be robust for TIDI.

[18] TIDI raw spectra also include significant channel-to-channel sensitivity variations induced by the optical fibers that are used to transfer light from the telescopes to the etalon. *Killeen et al.* [1999] and *Skinner et al.* [2003] show that the intensity variations between adjacent fiber structures in a telescope scene may reach 30% of the peak signal level. Careful weekly white light normalization calibration runs are conducted to model the channel-to-channel sensitivity of TIDI. The telescope scenes are exposed to Rayleigh scattered

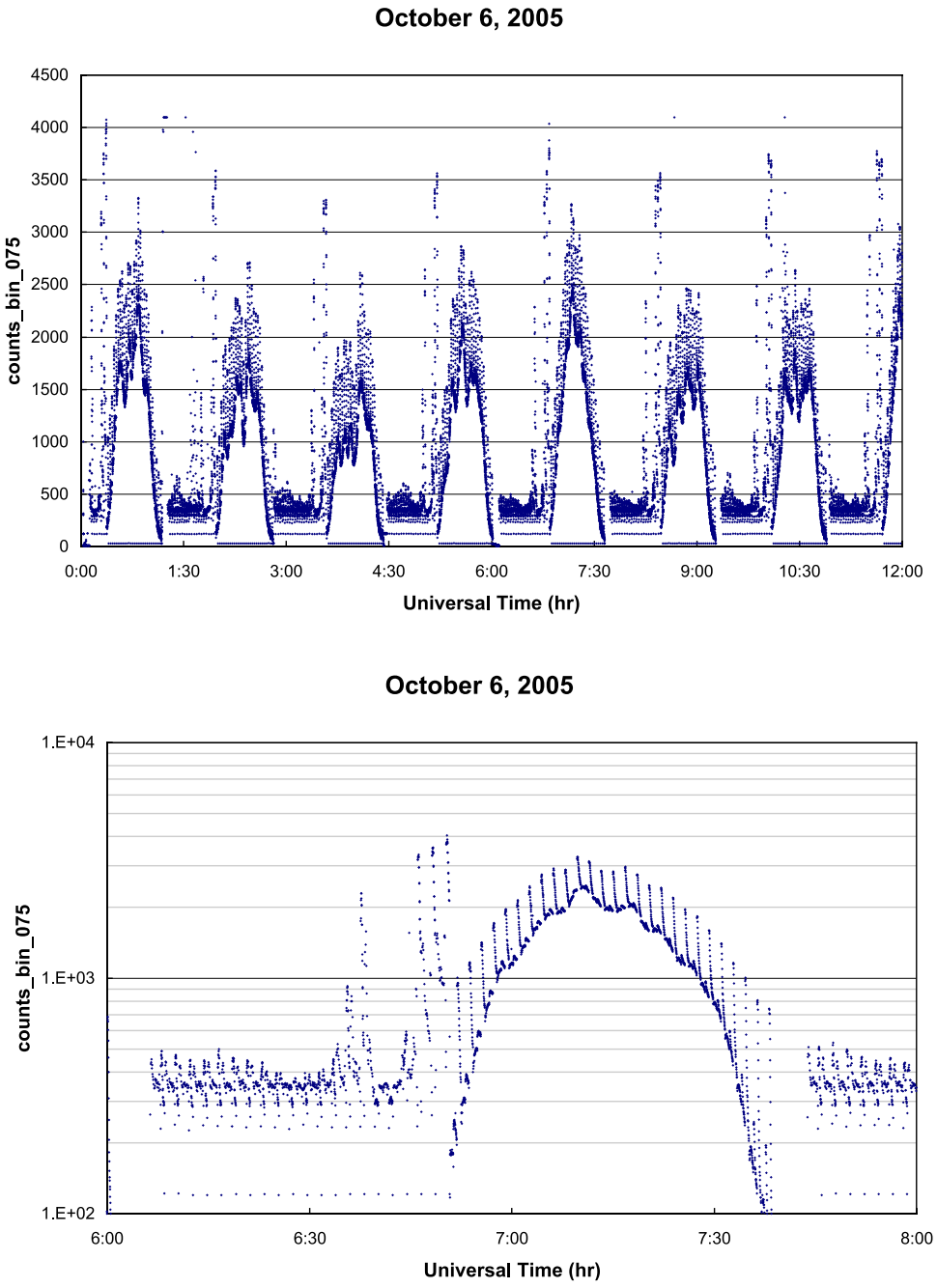

Figure 9. Level 0 data showing the response of channel 75 for (top) a 12-hour period and for (bottom) a shorter 2-hour period. Dayside data have a higher background than those acquired at night. The dark count changes between day and night due to a gain level change. Data gaps at dusk indicate periods when telescope shutters were closed for calibration lamp runs. The detector response during a vertical scan (bottom) implies that a TIDI cycle begins at the bottom of an airglow layer and ends after passing through the top of the layer.

sunlight in a controlled fashion to estimate the relative sensitivity of the individual channels. This approach also measures the cross-talk scattering in each spectral channel. Scattering is modeled by an exponential dropoff away from any specific channel. In this model, the response B on channel j to light impinging on channel i is given by

$$Bj = Ni^*(1 + a^* \exp(-c(j)^*\mathrm{abs}(i-j)))/S,$$

where Ni is a normalization constant that varies from channel to channel, a is a constant (a = 0 for no scattering), and c (j) = α for $j < i$; c (j) = β for $j > i$ is the exponential dropoff rate, $\alpha \neq \beta$, and S is the sum of the expression in parenthesis over j. The dropoff is different for channels on opposite sides of channel i. A matrix consisting of the response for all channels is constructed from a normalization calibration run. The inverse of this matrix is then applied to each airglow spectrum correcting the spectrum for both

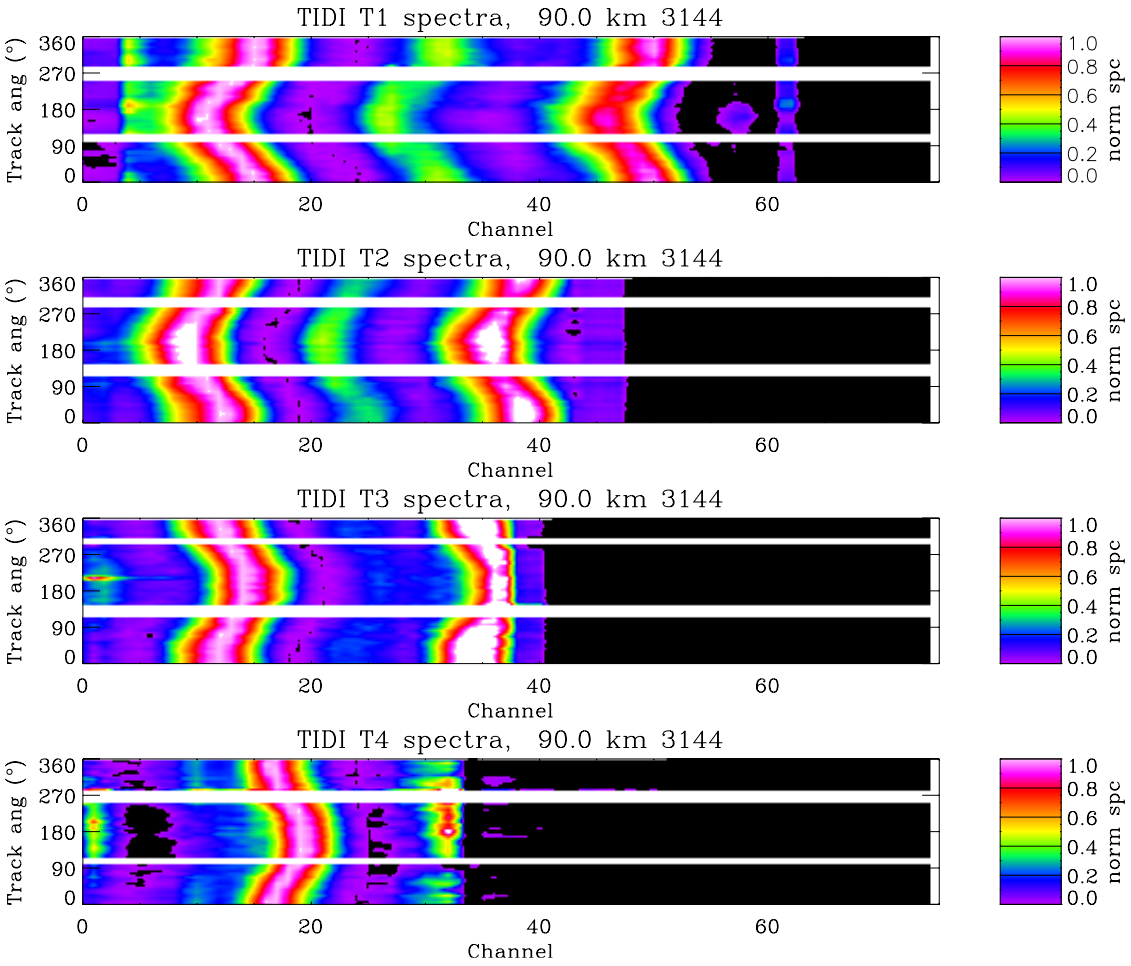

Figure 10. Daily summary of TIDI O_2 spectra for day number 144, 2003. Spectra are shown color coded as a function of tangent point track angle and channel number for all four telescopes. The display includes data for 90.0 km only. Spectral peaks appear as brighter colors in this normalized representation. The dark regions on the right are not included in any further analysis, nor are the short seam regions on the far left.

channel-to-channel sensitivity variations and to scattering cross talk. Finally, the spectrum is converted to absolute units based on prelaunch calibrations. Figure 10 summarizes the result of background and normalization corrections for one TIDI day. Here, spectra are shown in a color coded format, with the brighter colors referring to spectral peaks. The spectra are shown as a function of tangent point track angle and channel number. Track angle is 0 and 180 at the equator, with 90 and 270 referring to the northern and southernmost tangent point latitudes, respectively.

[19] The line of sight velocity is then determined separately for each telescope field. The approach is similar to that described by *Killeen and Hays* [1984]. For TIDI, the instrument function is modeled with a Fourier series representation based on prelaunch measurements of the etalon gap and reflectivity. Including the broadening due to the finite field of view, etalon plate roughness, and the finite aperture size associated with the detector pixels modifies the Airy function describing the instrument. Doppler broadening of airglow spectra assumes a value of 200 K for the atmospheric temperature, representative of the MLT region. The instrument function is convolved with a modeled O_2 spectrum appropriately corrected for filter transmission, and the resulting nonlinear fitting function is linearized in a Taylor expansion of the unknowns (wind, signal brightness, continuum background). This operation results in a set of linear functions that may be solved for the unknowns using traditional linear least squares techniques in an iterative fashion. Results for one TIDI day are shown in Figure 11. Geophysical parameters are shown as a function of tangent altitude and Universal Time for line of sight velocity (top), the $\log_{10}$ of line of sight brightness (middle), and the uncertainty of the velocity in the fit (bottom). The line of sight is at 45 degrees to the satellite velocity vector and its azimuth is cyclically repeatable as TIMED orbits the Earth. The component of the horizontal velocity along the line of sight is between ±100 m/s with an uncertainty ranging from 5 to 25 m/s depending upon signal brightness and suitability of the Gaussian fitting function. The uncertainty of the fit is strictly the statistical variance of each quantity, due primarily to Poisson noise, and is recovered from the diagonal components in the covariance matrix.

[20] The measured wind, v_m, determined from spectra such as those shown in Figure 10, consists of several

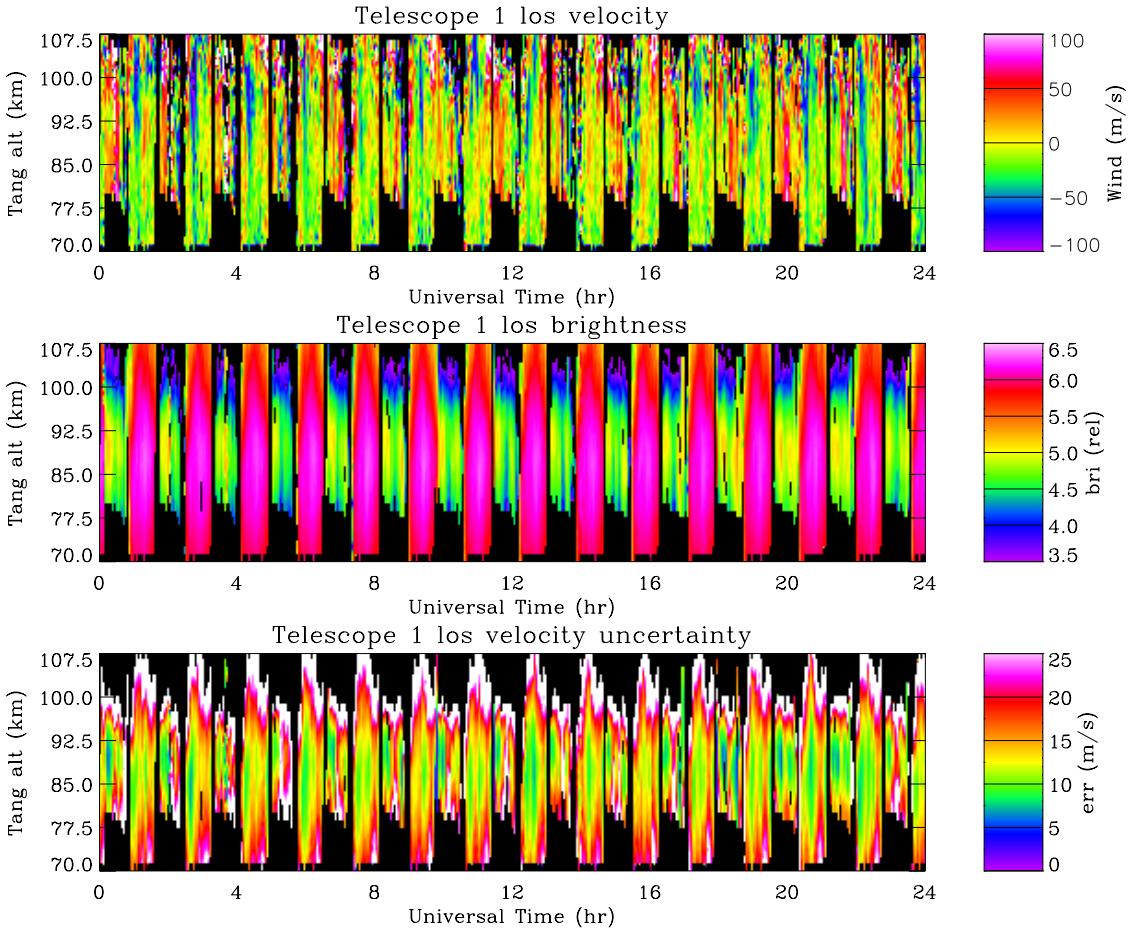

Figure 11. Level 1 geophysical results for day number 144, 2003, telescope 1. (top) Line of sight velocity, (middle) line of sight brightness, (bottom) velocity uncertainty.

satellite-induced effects as well as the geophysical wind, v_{los}. A full accounting of the line of sight velocity includes [*Burrage et al.*, 1993] (1) shifts of the "zero" wind position, $v_0(\nu, tel)$, due to instrument temperature fluctuations, $\alpha(T - T_0)$, (2) shifts of the "zero" wind position due to long term instrument drift, f(t), (3) shifts of the "zero" wind position due to the component of the spacecraft velocity along the line of sight, $v_s\cos\xi$, (4) shifts of the "zero" wind position due to the component of Earth rotation along the line of sight, $(2\pi R_E/T_E)\sin\psi\cos\theta$, and (5) the true line of sight geophysical wind, and may be written as

$$\text{Here } v_m = v_{los} + v_0(\nu, tel) + \alpha(T - T_0) + f(t) + v_s\cos\xi + (2\pi R_E/T_E)\sin\psi\cos\theta.$$

The "zero" wind position is completely determined by TIDI, and is dependent upon the emission feature observed, denoted by the peak frequency transmitted by the sampling interference filter, ν, and the specific telescope scene, denoted by the identification, *tel*. Satellite induced shifts of the "zero" wind position occur due to the motion of the observing platform, related to the orbital speed of the satellite, v_s, modified by the angle between the satellite velocity vector and the line of sight of the measurement, ξ. In addition, the airglow volume viewed by TIDI is different from one integration to the next and rotates about the Earth at a speed determined by the Earth's radius, R_E, and rotation period, T_E, and is a function of the tangent point latitude, θ, and the azimuth of the line of sight, ψ, of the measurement. The satellite environment also introduces temperature fluctuations of nonthermally controlled components of TIDI, and the "zero" wind shift associated with this affect is nominally described by a linear relationship between the temperature difference, $(T-T_0)$, from a reference temperature, T_0, modulated by a linear coefficient, α. The etalon is thermally controlled and does not introduce a contribution to daily variations in measured winds. Orbital operation also introduces a long-term drift into the measured velocity, denoted by f(t), a function of time, t. Wind shifts due to temperature fluctuations in components along the TIDI optical path follow the satellite beta angle cycle, as illustrated by Figure 12. Here, the mean temperature of the detector housing window, shown with one standard deviation error bars, follows a generally repeatable cycle as a function of solar beta angle. Finally, shifts in the "zero" TIDI wind follow a long-term trend that is monitored by daily calibrations as illustrated in Figure 5. These latter shifts are related to gradual outgassing of the satellite, primarily the sublimation of water.

[21] A large fraction of the shift in the spectral peaks shown in Figure 10 along an orbital track is caused by

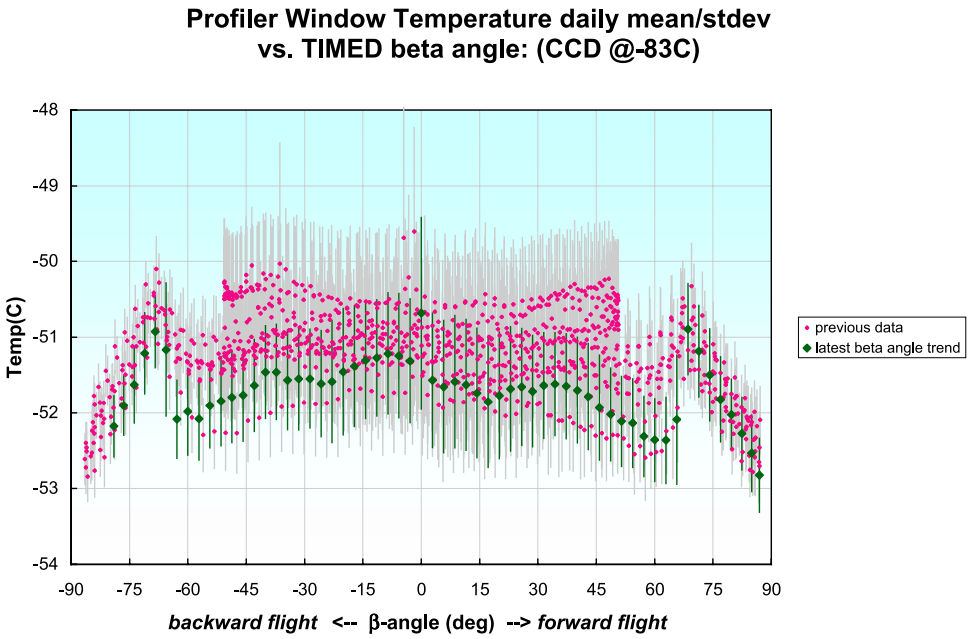

Figure 12. The daily temperature variation of the detector housing window, shown with one standard deviation error bars, as a function of solar beta angle. Satellite maneuvers occur near zero degree beta angle.

nongeophysical variation in the measured line of sight wind. One free spectral range, in terms of speed, is approximately 5200 m/s, covering roughly 30 channels for telescope 1. Though the satellite speed is ~7500 m/s, its variation along an orbital track is ~30 m/s due to the slight variance away from a perfectly circular orbit. The largest contribution to variation along track is due to the Doppler shift associated with the component describing Earth rotation, ~400 m/s. Effects due to temperature fluctuations are not evident in one orbit since thermal time constants for TIDI are many hours to nearly a day in length.

[22] The propagation of uncertainties in the measured wind due to satellite-induced changes influenced the design of TIDI. An accurate knowledge of the spacecraft velocity vector and the angle between a telescope's line of sight and the velocity vector are necessary to reduce the propagation of error in this component. The satellite speed is known to 0.25 m/s, while the spacecraft attitude angles (roll, pitch, and yaw) are known to 0.01 degree. The telescope pointing elevation and azimuth angles are known to 65 and 30 arcsec, respectively. As a result, the line of sight velocity uncertainty introduced by uncertain knowledge of the spacecraft velocity along the line of sight provides a random error of about 1.5 m/s.

[23] The major source of uncertainty in measurements of wind in the MLT is due to the "zero" wind estimate. This is a systematic error that is introduced into the measurement of the geophysical line of sight wind and is a persistent problem for all orbital-based Doppler wind experiments. Initial estimates for the spectral location of the "zero" wind consider dynamical assumptions [*Thayer*, 1990; *Carr et al.*, 1992; *Hays et al.*, 1992; *Burrage et al.*, 1993]. The next level of sophistication considers ground-based validation experiments of coincident satellite limb views in common volume elements [*Killeen et al.*, 1984; *Burrage et al.*, 1996; *Gault et al.*, 1996]. Finally, the most successful validation efforts to describe the "zero" wind consider combined satellite observations [*Burrage et al.*, 1997]. For TIDI, the estimate of the spectral location of "zero" wind is a function both of the observed spectral feature and the telescope employed in the measurement. In the current study, the "zero" wind position, $v_0(\nu, tel)$, is modified to vary on a daily basis by including both the temperature-dependent shift and the long-term drift, all assumed to create a systematic error in the geophysical wind measurement. This is accomplished for each telescope by determining the daily mean line of sight wind along the orbital track for an altitude range that is common to both dayside and nightside observations and then removing the mean from the daily data set. In this way, daily fluctuations due to thermal variations of the satellite are removed from the analysis. Comparisons with simple model data suggest that the "zero" wind calculated in this fashion is within 0–10 m/s of the true "zero" wind.

2.2.4. Level 2 Product

[24] The Level 2 product is constructed independently per telescope and is the result of an inversion of Level 1 airglow spectra accumulated over an altitude scan. The apparent Doppler shift, determined in the Level 1 TIDI data product, is a weighted average along the line of sight of the velocity component at each tangent altitude. It is possible to invert all apparent velocity measurements accumulated in a limb scan to form an altitude profile of the line of sight wind, recognizing that the measurements are mathematically described by an Abel integral equation [*Hays and Roble*, 1968], but it is generally agreed that this simple inversion will amplify the random noise in the retrieved winds. Consequently, this fault has led to the development of more robust techniques [*Hays et al.*, 1988]. The procedures employed to invert limb scans to extract vertical wind

profiles for both HRDI [*Ortland et al.*, 1995] and WINDII [*Gault et al.*, 1996] make use of constraints that reduce the noise sensitivity in an exact solution. Since the airglow spectral measurements are described by Poisson statistics, it is generally accepted that a solution to the inversion problem must lie within the experimental error of the observations, providing great flexibility in the choice of a solution. The basic equations and concepts are carefully described by *Rodgers* [1976] and developed for limb emissions by *Marks and Rodgers* [1993]. Essentially, the collection of spectra in an altitude scan performed by TIDI, represented by the vector $\mathbf{Y_{los}}$, is related to a mathematical representation of the spectra, vector **f(x)**, that represents the physics of the atmospheric measurements convolved with the instrument function, all based on the true geophysical parameters, $\mathbf{x}$.

$$\mathbf{Y_{los}} = \mathbf{f}(\mathbf{x}) + \varepsilon.$$

The uncertainty in the measurements is described by ε. A forward model, $\mathbf{Y}$, is produced based upon the instrument, the atmospheric physics, and a virtual data set to constrain the model, $\mathbf{x_a}$, in order to create a best guess of the geophysical parameters, $\mathbf{x}'$.

$$\mathbf{Y} = \mathbf{f}(\mathbf{x_a}, \mathbf{x}').$$

Implicit in the inversion is the assumption that during the finite time necessary to acquire the limb scan the atmosphere has not changed. The inversion also assumes that the atmosphere is spherically stratified. The use of an a priori, or virtual, estimate of the geophysical parameters may be considered as simply using the weighted average of two independent values of $\mathbf{x}$ in the forward model calculations, one being $\mathbf{x_a}$ and the other $\mathbf{x}'$. Its real advantage comes in the calculation of the uncertainty, or total error covariance, which now includes the covariance of the a priori term, and constrains the final solution to form a well-posed problem. In terms of Doppler shift determination, the constraint is based partially upon a climatological model of the atmosphere, though constraints may also take the form of vertical smoothing to remove unrealistic high-frequency components or of horizontal smoothing based on the expectation that adjacent altitude profiles should be correlated.

[25] The retrieval of geophysical information from $\mathbf{Y_{los}}$ is based on minimizing the difference between $\mathbf{Y_{los}}$ and $\mathbf{Y}$ as a function of $\mathbf{x}'$. The forward model, $\mathbf{Y}$, may be expanded in a Taylor series about the estimate $\mathbf{x}'$,

$$\mathbf{Y} = \mathbf{f}(\mathbf{x}') + \partial\mathbf{f}/\partial\mathbf{x}' + \ldots$$

and an updated $\mathbf{x}'$ may be written as a function of the a priori estimate plus a perturbation term resulting from the first estimate. A new difference, or chi-squared value, is determined from the improved estimate and the iteration continues until convergence is obtained. In practice, the first-order perturbation kernel is only computed once and includes the effect of self-absorption of O_2 At (0,0), which becomes important at the lowest altitudes in the inversion. An example of wind recovery with this technique may be found in the work of *Ortland et al.* [1996], who describe the inversion process, with detailed equations, that is used to extract stratospheric winds from HRDI observations.

[26] The errors reported for the TIDI Level 2 product are the sum total of two components. The first component is due to the random measurement error and the other is due to the a priori information. As expected, the total error is dependent upon the final form of the constraints used in the inversion.

[27] Figure 13 displays a daily average result from the Level 2 TIDI analysis product. Since the TIMED orbit does not vary significantly in terms of Local Solar Time coverage as a function of track angle between adjacent orbits, as suggested by Figure 11, it is extremely useful to coadd the geophysical products from individual orbits to construct daily averages. Statistically averaged data, binned in a similar fashion, form a significant core of the primary results from the analysis of HRDI and WINDII data products [*McLandress et al.*, 1996; *Fleming et al.*, 1996]. Though TIDI acquires more than 50,000 spectra per telescope per day, the number of unique vertical wind profiles from limb scans in the Level 2 product is significantly less. A limb scan requires ~100 s to complete and since TIMED orbits the Earth in ~100 min, only ~60 altitude scans per telescope are acquired by TIDI during one orbit. Track angle, or the true anomaly of the orbit, is a natural coordinate by which to bin satellite data. It does not suffer from any latitude ambiguity near the poles, and since the altitude bins are evenly separated in time, they are also evenly separated in track angle. In Level 2, the track angle as well as the geolocation of the vertical scan is determined by the mean temporal and spatial characteristics of the ensemble of spectra used in the inversion. The track angle bin width is chosen to collect between 15 and 20 samples per day, while the altitude spacing is determined by the output grid width of the Level 2 product, 2.5 km. As a result, meaningful statistical variances may be extracted from the daily averaged product as shown in Figure 13. The top panel displays the altitude profile of the mean line of sight velocity from the Level 2 inversion for telescope 1 for day number 144 of 2003, the middle panel displays the corresponding volume emission rate, and the bottom panel displays the standard deviation corresponding to the top panel. Examination of the volume emission rate profile average clearly delineates dayside and nightside observations, which is useful in understanding the wind mean and variance. The line of sight wind displays a minimum between 75 and 80 km on the dayside, with another local minimum near 100 km at track angles representative of low to middle latitudes. At high latitudes (track angles near 90 and 270), the line of sight wind profile indicates a maximum above 100 km, suggesting a significant change in the vertical wavelength of the wind as a function of latitude. This is expected as the tidal characteristics of the neutral wind change from diurnal at low latitudes to semidiurnal at higher latitudes in the mesosphere and lower thermosphere. The nightside winds show more structure and are approximately symmetric about the equator (track angle = 180 degrees) and roughly asymmetric with the dayside at low and middle latitudes, also suggestive of the diurnal tide. The standard deviation of the winds should be an accurate representation of geophysical noise on a global scale. TIDI operates at nearly 100% duty cycle implying that the

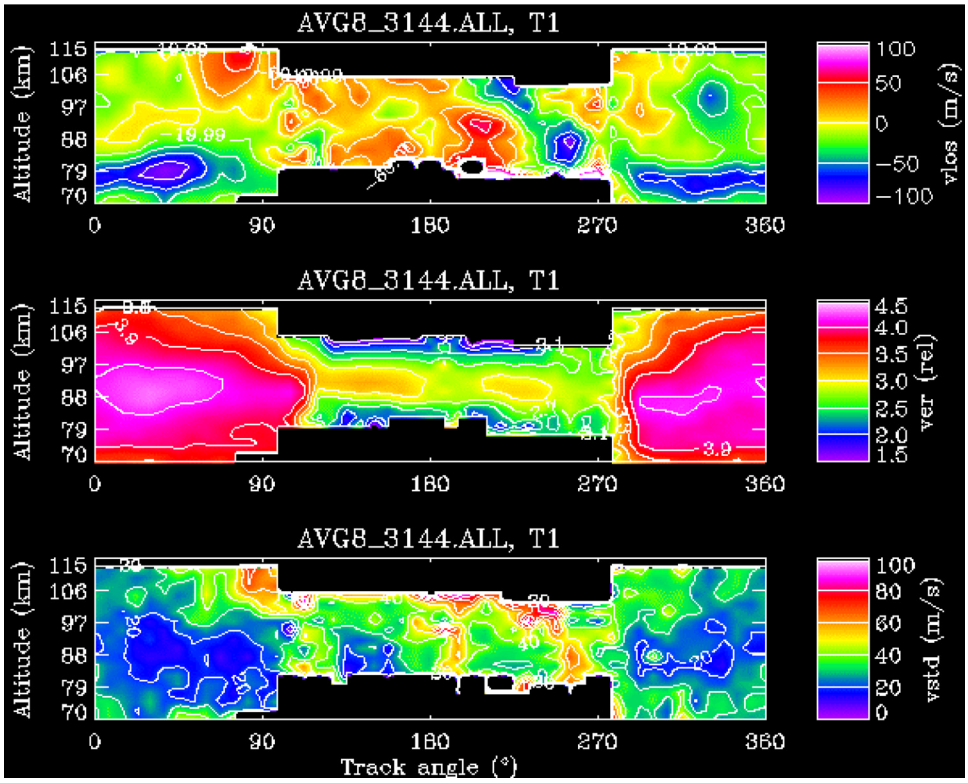

Figure 13. Level 2 geophysical results for day number 144, 2003, telescope 1. The data have been binned as a function of track angle and altitude. (top) Inverted line of sight velocity, (middle) volume emission rate, (bottom) standard deviation of the inverted line of sight velocity.

longitude coverage for each wind bin represents measurements that have been accumulated globally and with even longitude separation, ~24 degrees. The higher values in the track angle range 180 to 270 degrees are associated with poorer quality spectra acquired while the satellite is within the South Atlantic Anomaly. For much of the observed track angle/altitude range, the statistical deviation lies in the range 20–40 m/s. This geophysical variance is very similar to the values observed for daily binned averages with HRDI and WINDII winds [*Burrage et al.*, 1996].

[28] The annual repeatability of the TIMED orbit allows direct comparisons of geophysical parameters between different years. Figure 14 displays a track angle/altitude map of the O_2 At (0,0) volume emission rate for day number 144 for 2002 to 2005. The Local Solar Time coverage is identical in all panels, though the nightside period of 2002 contains poorer quality data related to operating through spacecraft maneuvers associated with SABER pointing calibrations. The beta angle in all cases is near zero degrees indicating that the local time on the dayside is close to noon, while on the nightside near midnight. The gradual decrease in the emission layer height as the track angle increases through the nightside (latitude changes from high northern to high southern) is repeatable, as well as the locations of the peak dayside emission rate in terms of track angle and altitude.

2.2.5. Level 3 Product

[29] The Level 3 TIDI product consists of altitude profiles of the horizontal neutral wind components. These are constructed separately for the coldside and the warmside from appropriately combined line of sight winds and placed onto a standard TIMED grid. The precession rate of TIMED allows a reconstruction of the apparent variation of the neutral wind as a function of latitude, local solar time, and altitude by combining all measurements acquired during a ~60-day yaw cycle. There will always be some gaps in the coverage as the local time at the tangent point will never include all local times for all latitudes and altitudes. The reconstruction result should not be confused with a true global time/space map of the winds for any given date, which presently, cannot be constructed with any real precision from any collection of data sets. The data cube in local time, latitude, and altitude, which is built from the total collection of TIDI measurements, contains only six unique reconstructions per year corresponding to individual periods separated by yaw maneuvers. As previously described, however, these reconstructions are for the same calendar periods for each year and provide a unique and simple technique to intercompare the winds at the same place but different years.

[30] Figures 15 to 17 display representative results for the meridional component of the horizontal neutral wind. Tidal structure in the MLT is more pure and pronounced in the meridional component. The zonal wind component in a composite wind reconstruction may be aliased with a strongly varying zonal mean wind, such as that due to the mesosphere semiannual oscillation [*Hays et al.*, 1994], resulting in a more confused reconstruction of the tides. The strong cell structure at lower latitudes in Figure 15 is due to the existence of the 1,1 mode of the diurnal tide in

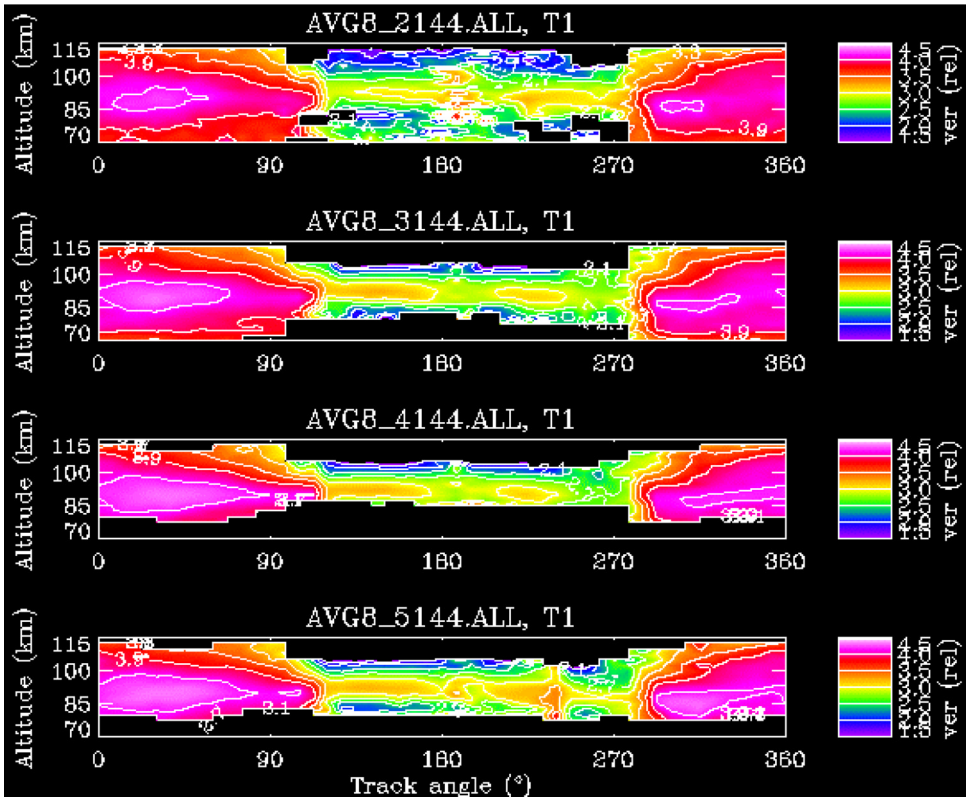

Figure 14. Daily averaged volume emission rate of O_2 At (0-0) as a function of track angle for the same date, day number 144, for consecutive years. The 2002 data set is slightly contaminated due to spacecraft maneuvers related to SABER pointing calibrations. The general features of the volume emission rate profiles are repeatable, including a slow altitude decrease in the peak altitude of the volume emission rate as the sampling volume on the nightside changes from high northern to high southern latitudes.

the MLT. The amplitude of the 1,1 mode shows significant interannual variation that is due solely to geophysical variation and is not due to differing spacecraft viewing geometry from one year to the next. The tidal structure is seen to vary as a function of latitude in Figures 16a and 16b. At low latitudes, the tide in the MLT region has a strong diurnal component, while at high latitudes the semidiurnal tide is dominant. The different tidal components have different vertical wavelength, easily seen in the altitude/local solar time displays. At low latitudes, the diurnal character of the tide at 90 km altitude is evident in the display of Figure 17. The day/night coverage is more complete for the warmside TIDI data set in the January to March yaw period, though during this period the warmside can only point to southern high latitudes. The change to a semidiurnal wind occurs poleward of ~45S latitude.

[31] Validation of the TIDI winds against those acquired by UARS also permits the characterization of the MLT region for the period 1991 to present. Figure 18 displays the interannual variability in the meridional component of the horizontal neutral wind at 20N, determined simply as the mean, per yaw cycle, of the meridional wind measurements between 6 and 18 hours Local Solar Time. HRDI winds are shown for the period 1991 to 2000, with TIDI winds shown from 2002 to present. The dominant structure at this latitude is the diurnal tide with a vertical wavelength of between 23 and 25 km.

3. Long-Term Variability of the Diurnal Tide in the Tropics

[32] The most dominant dynamical feature in the MLT region is the migrating diurnal tide in the tropical upper atmosphere [*Hays et al.*, 1994; *Burrage et al.*, 1995]. The classical representation of this tidal feature suggests cells that are centered near 20 degrees latitude, with the meridional component of the horizontal wind being asymmetric about the equator and maximizing in amplitude between 90 and 100 km altitude. This feature is represented theoretically as the (1,1) Hough mode component. The diurnal tide in the tropical MLT displays a strong and distinct semiannual behavior, peaking at the equinox dates with amplitudes approaching 100 m/s, while decreasing significantly in strength during the solstice dates. The vertical wavelength of the (1,1) tide is 23 km [*Hays et al.*, 1994] with a small altitude-dependent variation. It is generally believed that this migrating diurnal tidal component is generated in the troposphere by solar heating and propagates upward into the MLT region. *Burrage et al.* [1995] concluded that gravity wave stressing is required to describe the seasonal behavior of the diurnal tide.

[33] The synoptic observational strategy of TIDI has permitted continuous and detailed sampling of the wind

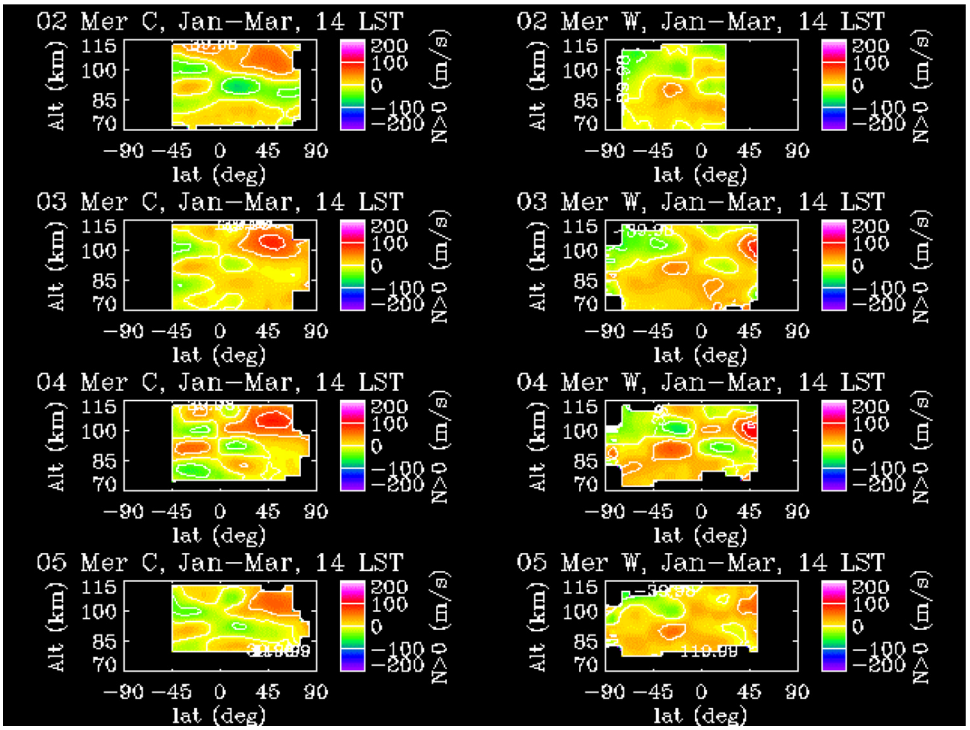

Figure 15. The combined meridional wind from the mid-January to mid-March yaw cycle for the years 2002 to 2005 at 14-hour Local Solar Time as a function of altitude and latitude. Both the cold and the warm side meridional wind component are shown constructed from the appropriate telescopes. The color code is chosen to highlight the asymmetric nature of the diurnal tide about the equator, and the interannual variation in its magnitude.

field in the MLT on a daily basis from early 2002. However, unlike ground-based wind observations which can sample a volume of atmosphere as the Earth rotates beneath it and easily characterize the diurnal amplitude and phase, TIMED samples relatively the same local solar time slice in each orbit on any specific day. Consequently, the determination of diurnal tide characteristics in MLT winds from TIDI requires a nontraditional approach. A significant study was performed by *Hays et al.* [1994], assuming that the diurnal migrating tide in the tropics was solely represented by the classical (1,1) Hough mode, and applied this approximation to nearly 2 years of HRDI MLT wind measurements. The amplitude of the diurnal tide was estimated using a two-step approach employing all wind data acquired at latitudes within 35 degrees of the equator and over the entire observable MLT altitude range. The technique was applied solely to the meridional wind, since the zonal component of the horizontal wind also included a large mean offset and a major contribution from the mesospheric semiannual oscillation [*Lieberman et al.*, 1993]. The first step was to fit a 24-hour sinusoidal variation to a composite Local Solar "day" acquired during yaw cycles that included samples on and near an equinox date. This fitting resulted in an altitude-dependent representation of the amplitude of the migrating diurnal tide, $\zeta(z_j)$, that was then incorporated into a parameterization of the (1,1) meridional Hough mode component, $V(\theta_i)$,

$$M_{ij} = \zeta(z_j)V(\theta_i)\{\mathrm{A}\ \cos[2\pi(z_j/23 + t_i/24)] + \mathrm{B}\ \sin[2\pi(z_j/23 + t_i/24)]\},$$

where the satellite meridional wind measurements are given by M_{ij} at altitude z_j and Local Solar Time t_i. A least squares fit for each day of wind measurements then provided estimates for the unknown parameters A and B, and with the standard conversion, the amplitude and the phase of the classical (1,1) Hough mode component.

[34] Figure 19 displays the diurnal tidal amplitude results for the entire TIDI mission using the technique of *Hays et al.* [1994]. The trend displayed by the amplitude show distinct maxima each year during the March equinox, with somewhat less distinct maxima during the September equinox. The greatest diurnal tide is observed during March 2004. The interannual variability is similar to that observed by *Burrage et al.* [1995], where the largest maxima were seen in 1992, 1993, and 1995 with a weaker peak in 1994. Though TIDI wind results continue to undergo validation efforts, Figure 19 indicates that both TIDI and HRDI observe similar annual variations in the strength of the tropical migrating diurnal tidal amplitude when the wind data are viewed as daily averages.

[35] A quantitative estimate of the interannual variability of the diurnal tide can be made by fitting the seasonal behavior with a semiannual and an annual dependence, the latter necessary since the September peak falls approximately 10 days after the equinox date while the March peak is essentially at equinox. Table 3 summarizes the fitting results for the TIDI mission. The diurnal tide has the greatest amplitude in 2004 but is not as well developed in 2005. The results for 2002 are biased somewhat as Level 2 TIDI meridional winds are not available until day 59, 2002. The interannual variability is similar in degree to that described

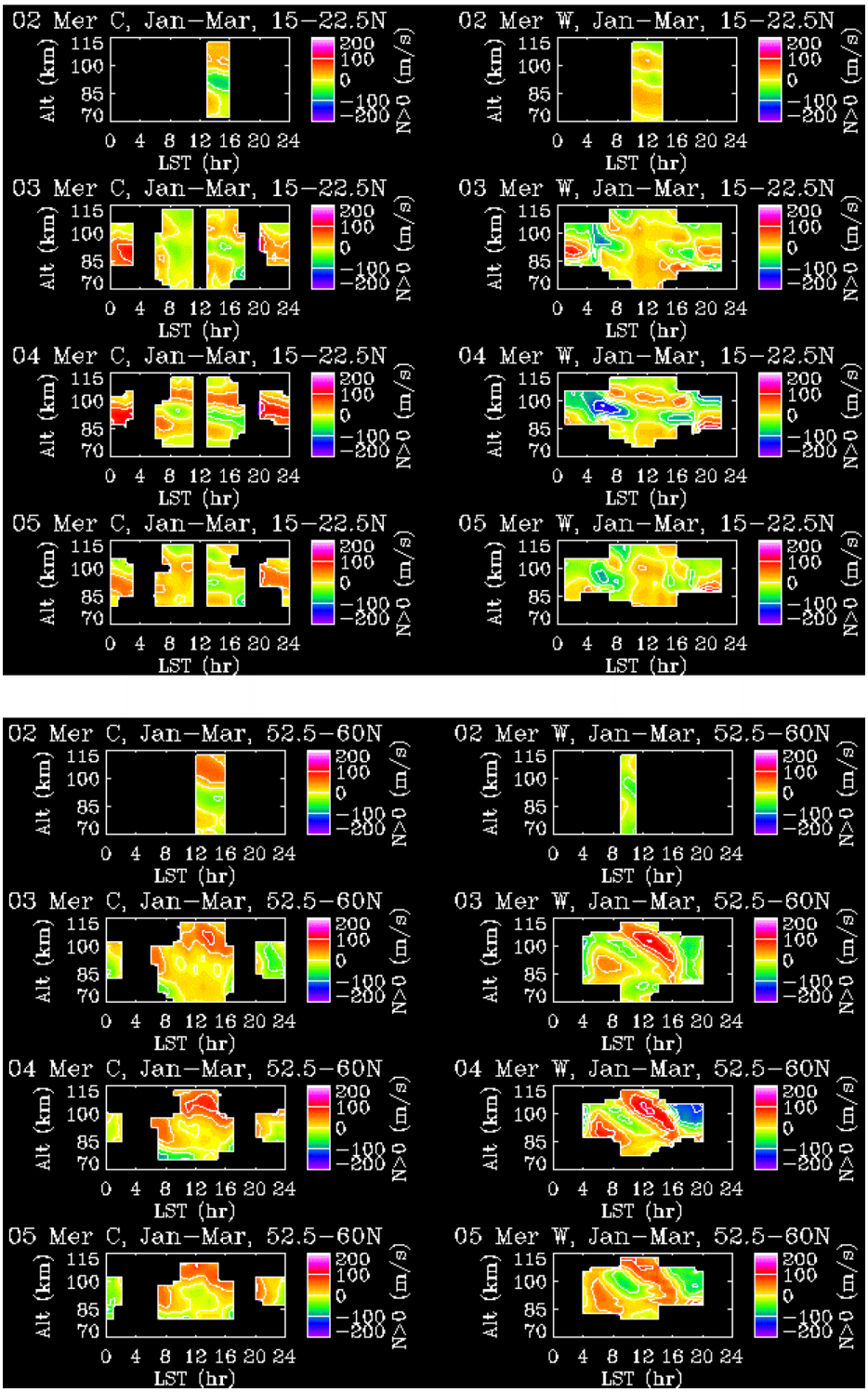

Figure 16. The combined meridional wind from the mid-January to mid-March yaw cycle for the years 2002 to 2005 for the latitude ranges (a) 15–22.5 deg N and (b) 52.5–60 deg N, as a function of altitude and Local Solar Time. The two views describe the diurnal tide at lower latitude and the semidiurnal tide at higher latitude.

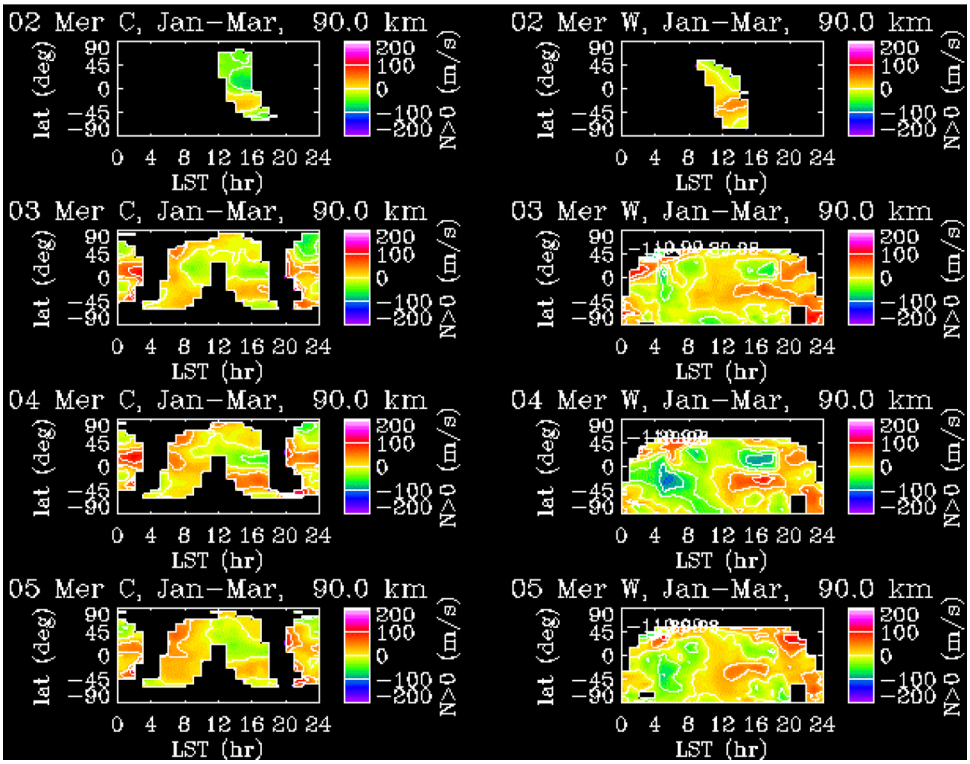

Figure 17. The combined meridional wind from the mid-January to mid-March yaw cycle for the years 2002 to 2005 at an altitude of 90 km as a function of latitude and Local Solar Time. The current operational mode did not start until late February 2002. The missing regions in the cold and warm side displays correspond to latitude/time coordinates that are outside the viewing geometry for a TIMED yaw cycle.

by the HRDI results of *Burrage et al.* [1995] and the ground-based observations of *Vincent et al.* [1988]. In a recent numerical study employing a lower atmosphere gravity wave source to create a quasi-biennial oscillation (QBO) at ~30 km altitude, *Mayr and Mengel* [2005] have shown that at MLT heights the QBO can modulate the equinoctial seasonal maxima by up to 30% between adjacent years. Further investigations are continuing with UARS and TIDI data to better understand the long-term variability of the diurnal tide in the tropics and will be reported elsewhere.

4. Conclusions

[36] This paper has presented an overview of the TIMED Doppler Interferometer that has been flying aboard TIMED since late 2001. The operational characteristics of TIDI

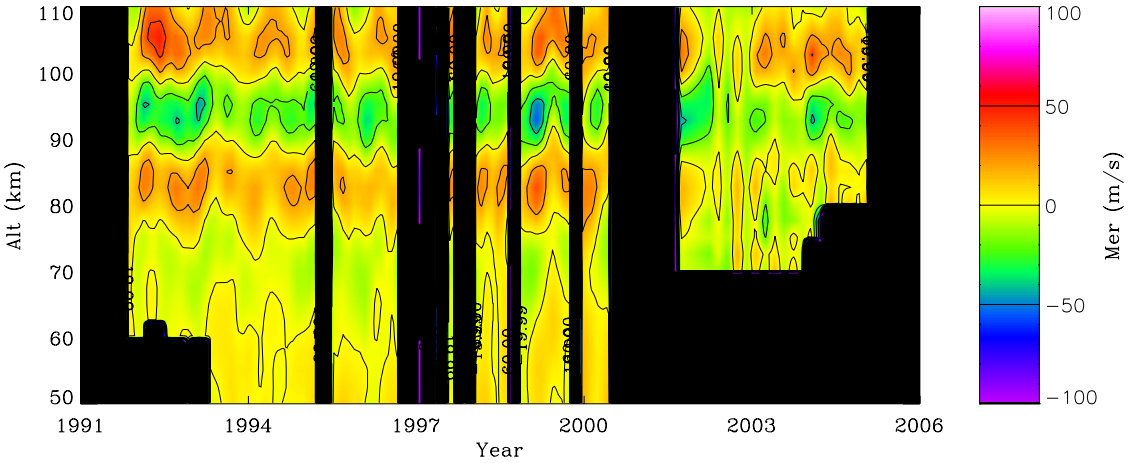

Figure 18. The meridional wind averaged over yaw cycles as a function of altitude and year. The yaw cycle average has been calculated only for data acquired between 6 and 18 hours Local Solar Time. HRDI measurements contribute to the period 1991 to 2000, and TIDI measurements to 2002 to present.

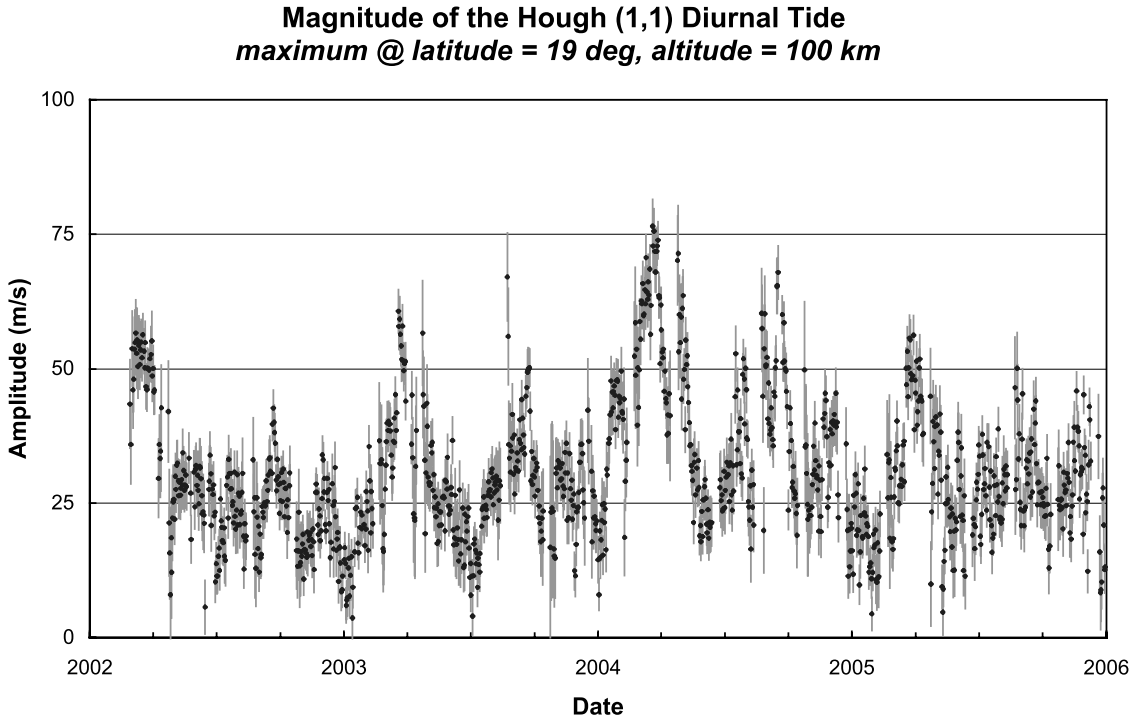

Figure 19. The amplitude of the classical migrating diurnal (1,1) Hough mode tide in the tropics. The uncertainty of the least squares fit is shown as an error bar for each daily point.

indicate (1) satisfactory signal to noise ratio in individual raw spectra, (2) statistical uncertainties as low as ~5 m/s in fits to individual line of sight spectra, (3) zonal variances of 20–40 m/s in daily averaged winds, representative of the geophysical noise expected along a latitude circle, (4) small instrument random noise contributions, ~1.5 m/s, to the "zero" wind, and (5) the systematic daily bias in the "zero" wind introduced by satellite induced changes may be estimated by using the track angle mean of the daily geophysical line of sight wind.

[37] In particular, the data products that are available at different levels of analysis and sophistication, demonstrate that TIDI is capable of performing important dynamics observations of the MLT region with all data acquired from early 2002 to present. In comparison to previous missions, the unique capabilities of TIDI permit (1) studies of the tide in the altitude range 70 to 115 km from the equator to the pole, (2) studies of the interannual behavior of the MLT region by direct comparison of the wind fields from one year to the next, (3) the extension of the UARS dynamics measurements of the MLT from 1991 to the present permitting the characterization of long-term dependences, and (4) essentially constant viewing of the MLT region by a stable and reliable Fabry Perot interferometer.

[38] Initial scientific results from the entire mission indicate that the migrating diurnal tide is dominant in the tropics. Fitting of the classical (1,1) Hough mode to tropical MLT meridional winds indicate that the diurnal tide reaches maximum amplitude during March equinox of each year, with a lesser maximum during the September equinox. A significant interannual variability exists in the diurnal tide. Further investigations into the long-term behavior of the diurnal tide with HRDI and WINDII will provide new information on the climatology of the MLT region.

[39] The climatology of the MLT region can now be thoroughly studied using the data sets available from the HRDI and WINDII experiments from UARS and the new TIDI wind measurements from TIMED. Though there are inconsistencies in the comparisons between MLT winds deduced from ground-based radio frequency methods and satellite observations [*Burrage et al.*, 1996], the confidence gained from statistically similar results from direct intercomparisons between HRDI and WINDII suggest that further improvements can be made in empirical models of the MLT by using satellite data. Employing TIDI, along with HRDI and WINDII, can permit significant advances in representations of atmospheric dynamics such as the Hor-

Table 3. Summary of the Fit to the Daily Variation of the Diurnal Migrating Tide in the Tropics[a]

Year	Constant, m/s	Semiannual Amplitude, m/s	Semiannual Phase, days	Annual Amplitude, m/s	Annual Phase, days
2002	29.4 ± 0.5	8.4 ± 0.7	66.8 ± 2.4	10.2 ± 0.7	71.6 ± 4.1
2003	28.3 ± 0.5	9.8 ± 0.7	85.7 ± 2.0	1.6 ± 0.7	101.1 ± 24.5
2004	39.1 ± 0.6	13.6 ± 0.8	76.1 ± 1.8	7.0 ± 0.8	86.2 ± 6.9
2005	28.1 ± 0.5	6.4 ± 0.7	93.2 ± 3.3	2.3 ± 0.7	140.7 ± 18.9

[a]The regression fit provided a constant term as well as semiannual and annual amplitudes and phases.

izontal Wind Model [*Hedin et al.*, 1996] for the MLT region.

[40] The large variance in the daily MLT winds is also of great interest. Though a large part of the daily variation of the winds is purely tidal in origin, the MLT region is located between strong forcing mechanisms from above and below. Gravity waves become large in the MLT and "break," while ionospheric forcing from above, influenced by geomagnetic activity, may interact with the inherent tidal variation. Nonmigrating tidal structures and large planetary wave activity can also contribute to the natural geophysical variance in zonally averaged winds in the MLT. Both HRDI and TIDI have performed observations from opposite sides of the spacecraft flight path, and these data may yet be able to resolve longitudinal structure in the winds. By carefully characterizing the dominant migrating tidal behavior in the MLT, it should be possible to resolve nonmigrating tides and potentially, the contribution to dynamics from breaking gravity waves.

[41] **Acknowledgments.** This work was supported by NASA grants NAG5-5049 to the University of Michigan and NAG5-5334 to the National Center for Atmospheric Research.

[42] Lou-Chuang Lee thanks the two reviewers for their assistance in evaluating this paper.

References

Burrage, M. D., et al. (1993), Comparison of HRDI wind measurements with radar and rocket observations, *Geophys. Res. Lett.*, *20*, 1259–1262.

Burrage, M. D., M. E. Hagan, W. R. Skinner, D. L. Wu, and P. B. Hays (1995), Long-term variability in the solar diurnal tide observed by HRDI and simulated by the GSWM, *Geophys. Res. Lett.*, *22*, 2641–2644.

Burrage, M. D., et al. (1996), Validation of mesosphere and lower thermosphere winds from the High-Resolution Doppler Imager of UARS, *J. Geophys. Res.*, *101*, 10,365–10,392.

Burrage, M. D., W. R. Skinner, and P. B. Hays (1997), Intercalibration of HRDI and WINDII wind measurements, *Ann. Geophys.*, *15*, 1089–1098.

Carr, S. S., T. L. Killeen, and W. R. Coley (1992), Remote-sensing observations of F-region ion drift velocities using Dynamics Explorer-2 Doppler measurements of the $O^+(^2P)$ λ732.0 nm emission, *Geophys. Res. Lett.*, *19*, 1455–1458.

Fleming, E. L., S. Chandra, M. D. Burrage, W. R. Skinner, P. B. Hays, B. H. Solheim, and G. G. Shepherd (1996), Climatological mean wind observations from the UARS high-resolution Doppler imager and wind imaging interferometer: Comparison with current reference models, *J. Geophys. Res.*, *101*, 10,455–10,473.

Gault, W. A., et al. (1996), Validation of $O(^1S)$ wind measurements by WINDII: The WIND Imaging Interferometer on UARS, *J. Geophys. Res.*, *101*, 10,405–10,430.

Hays, P. B. (1990), Circle to line interferometer optical system, *Appl. Opt.*, *29*, 1482–1489.

Hays, P. B., and R. G. Roble (1968), Atmospheric properties from the inversion of planetary occultation data, *Planet. Space Sci.*, *16*, 1197–1198.

Hays, P. B., G. Carignan, B. C. Kennedy, G. G. Shepherd, and J. C. G. Walker (1973), The Visible-Airglow Experiment on Atmosphere Explorer, *Radio Sci.*, *8*, 369–377.

Hays, P. B., T. L. Killeen, and B. C. Kennedy (1981), The Fabry-Perot interferometer on Dynamics Explorer, *Space Sci. Instrum.*, *5*, 395–416.

Hays, P. B., V. J. Abreu, S. C. Solomon, and J.-H. Yee (1988), The Visible Airglow Experiment – A review, *Planet. Space Sci.*, *36*, 21–35.

Hays, P. B., and the HRDI science team (1992), Remote sensing of mesospheric winds with the High-Resolution Doppler Imager, *Planet. Space Sci.*, *40*, 1599–1606.

Hays, P. B., V. J. Abreu, M. E. Dobbs, D. A. Gell, H. J. Grassl, and W. R. Skinner (1993), The High-Resolution Doppler Imager on the Upper Atmosphere Research Satellite, *J. Geophys. Res.*, *98*, 10,713–10,723.

Hays, P. B., D. L. Wu, and the HRDI Science Team (1994), Observations of the diurnal tide from space, *J. Atmos. Sci.*, *51*, 3077–3093.

Hecht, J. H., A. B. Christensen, and J. B. Pranke (1985), High-resolution auroral observations of the OI (7774) and OI (8446) multiplets, *Geophys. Res. Lett.*, *12*, 605–608.

Hedin, A. E., et al. (1996), Empirical wind model for the upper, middle and lower atmosphere, *J. Atmos. Terr. Phys.*, *58*, 1421–1447.

Killeen, T. L., and P. B. Hays (1984), Doppler line profile analysis for a multichannel Fabry-Perot interferometer, *Appl. Opt.*, *23*, 612–620.

Killeen, T. L., R. W. Smith, P. B. Hays, N. W. Spencer, L. E. Wharton, and F. G. McCormac (1984), Neutral winds in the high latitude winter F-region: Coordinated observations from ground and space, *Geophys. Res. Lett.*, *11*, 311–314.

Killeen, T. L., et al. (1999), TIMED Doppler Interferometer, *Proc. SPIE*, *3756*, 289–315.

Lieberman, R. S., M. D. Burrage, D. A. Gell, P. B. Hays, A. R. Marshall, D. A. Ortland, W. R. Skinner, D. L. Wu, R. A. Vincent, and S. J. Franke (1993), Zonal mean winds in the equatorial mesosphere and lower thermosphere observed by the High Resolution Doppler Imager, *Geophys. Res. Lett.*, *20*, 2849–2852.

Marks, C. J., and C. D. Rodgers (1993), A retrieval method for atmospheric composition from limb emission measurements, *J. Geophys. Res.*, *98*, 14,939–14,953.

Mayr, H. G., and J. G. Mengel (2005), Interannual variations of the diurnal tide in the mesosphere generated by the quasi-biennial oscillation, *J. Geophys. Res.*, *110*, D10111, doi:10.1029/2004JD005055.

McLandress, C., G. G. Shepherd, B. H. Solheim, M. D. Burrage, P. B. Hays, and W. R. Skinner (1996), Combined mesosphere/thermosphere winds using WINDII and HRDI data from the Upper Atmosphere Research Satellite, *J. Geophys. Res.*, *101*, 10,441–10,453.

Niciejewski, R., T. L. Killeen, and M. Turnbull (1994), Ground-based Fabry-Pérot interferometry of the terrestrial nightglow with a bare charge-coupled device: Remote field site deployment, *Opt. Eng.*, *33*, 457–465.

Ortland, D. A., P. B. Hays, W. R. Skinner, M. D. Burrage, A. R. Marshall, and D. A. Gell (1995), A sequential estimation technique for recovering atmospheric data from orbiting satellites, in *The Upper Mesosphere and Lower Thermosphere*, *Geophys. Monogr. Ser.*, vol. 87, edited by R. M. Johnson and T. L. Killeen, pp. 329–337, AGU, Washington, D. C.

Ortland, D. A., W. R. Skinner, P. B. Hays, M. D. Burrage, R. S. Lieberman, A. R. Marshall, and D. A. Gell (1996), Measurements of stratospheric winds by the high resolution Doppler imager, *J. Geophys. Res.*, *101*, 10,351–10,363.

Rodgers, C. D. (1976), Retrieval of atmospheric temperature and composition from remote measurements of thermal radiation, *Rev. Geophys.*, *14*, 609–624.

Skinner, W. R., et al. (2003), Operational performance of the TIMED Doppler Interferometer, *SPIE*, *5157*, 47–57.

Thayer, J. P. (1990), Neutral wind vortices in the high-latitude thermosphere, Ph.D. dissertation, Univ. of Mich., Ann Arbor.

Vincent, R. A., T. Tsuda, and S. Kato (1988), A comparative study of mesospheric solar tides observed at Adelaide and Kyoto, *J. Geophys. Res.*, *93*, 699–708.

Yee, J.-H., E. Rodberg, R. J. Harvey, D. Kusnierkiewicz, W. Knopf, P. Grunberger, D. Grant, and G. Cameron (2003), Advanced technology and mission operations concepts employed on NASA's TIMED mission, *Proc. SPIE*, *5088*, 43–52.

M. Cooper, A. Marshall, R. Niciejewski, and W. Skinner, Space Physics Research Laboratory, University of Michigan, 2455 Hayward Street, Ann Arbor, MI 48109, USA. (niciejew@umich.edu)

D. Gell, Southwest Research Institute, 6220 Culebra Road, P.O. Drawer 28510, San Antonio, TX 78228-0510, USA.

T. Killeen, S. Solomon, and Q. Wu, National Center for Atmospheric Research, 3450 Mitchell Lane, Boulder, CO 80301, USA.

D. Ortland, NorthWest Research Associates, 14508 NE 20th Street, Bellevue, WA 98007, USA.